7591R1 - CORRECTION:

Geochemistry and boron isotope compositions of tourmalines from the granite-greisen-quartz vein system in Dayishan pluton, Southern China: Implications for potential mineralization

Zhuang Zhao [a,b], Xiaoyong Yang [a,b,*], Youyue Lu [c], Zunzun Zhang [c], Shanshan Chen [a,b], Chao Sun [a,b], Qi Hou [a,b], Yu Wang [a,b], Shuang Li [d]

[a] *CAS Key Laboratory of Crust – Mantle Materials and Environments, School of Earth and Space Sciences, University of Science and Technology of China, Hefei 230026, China*

[b] *CAS Center for Excellence in Comparative Planetology, Hefei 230026, China*

[c] *Wuhan Centre of China Geological Survey, Wuhan 430205, China*

[d] *Guangxi Key Laboratory of Hidden Metallic Ore Deposits Exploration, College of Earth Sciences, Guilin University of Technology, Guilin 541004, China*

Abstract

Tourmaline occurs widely within the Dayishan ore field, Nanling Range, and is associated with magmatic-hydrothermal rare metal mineralization. Four types of tourmaline are recognized: (1) tourmaline in coarse-grained monzogranite (Tur-G1); (2) tourmaline in medium-fine grained monzogranite (Tur-G2); (3) tourmaline aggregates associated with muscovite in greisen (Tur-Gr), showing a yellow core (Tur-Gry) and blue rim (Tur-Grb); and (4) quartz-vein-hosted tourmaline (Tur-V). In this study, we performed systematic investigations of in-situ boron isotopic and elemental compositions of tourmalines in different granite, greisen and quartz veins by EPMA and LA-MC-ICP-MS. Results show that almost all tourmalines exhibit schorl compositional affinity with extremely low Ca contents, high Fe/(Fe + Mg), and the calculated X-site occupancies in tourmalines show their affinities to alkali group. Substitution processes of major element variations are dominantly caused by $MgFe_{-1}$, $FeAl_{-1}$, (Ca, Mg) ($\square_{-1}$, Al_{-2}) and R $(Na, Mg)_{-1}$ exchange vectors. Based on geochemistry and petrology, Tur-G1, Tur-G2 and Tur-Gry precipitated from a boron-rich melt, while Tur-Grb and Tur-V crystallized from hydrothermal fluid. Many trace element concentrations overlap and most are < 10 ppm. The significantly higher contents of Sn and Zn and positive Eu anomaly reflect the influence of an external fluid. Magmatic tourmalines fall into a narrow range of $\delta^{11}B$ values between -15.58 ‰ and -14.09 ‰, indicating a single boron source of the granitic magma. Hydrothermal tourmalines display slightly lighter B isotopic compositions (-16.31 ‰ to -14.91 ‰), which are consistent with precipitation from externally-derived fluids with lighter boron. Based on the isotopic and chemical compositional evidence, Sn and Zn may come from the host rock rather than granite.

Keywords: Tourmaline; Boron isotope; Sn deposit; Nanling Range; Potential mineralization

Introduction

Tourmaline has been regarded as a reliable geochemical monitor for mineral exploration because it is a passive recorder of its depositional environment and is geologically widespread occurrence in different geological environments including magmatic, hydrothermal, detrital and metamorphic settings (Chaussidon and Appel, 1992; Henry and Dutrow, 1996, 2012; Trumbull and Chaussidon, 1999; van Hinsberg, 2011a, b; Drivenes et al., 2015; Duan et al., 2019). Moreover, tourmalines possess highly variable geochemical compositions and are stable over large P-T ranges, which make tourmaline an important tool in petrologic and ore genetic studies for constraining fluid compositions and hydrodynamics of geological processes (Jiang et al., 1997, 2002, 2004; Van Hinsberg et al., 2006, 2011b; Slack and Turmbull, 2011; Marks et al., 2013; Dutrow and Henry, 2011; 2018). Fractionations of ^{11}B and ^{10}B between fluid and granitic melt can assist in understanding the boron sources, hydrothermal fluids evolution and water-rock reaction (Marschall et al., 2009; Codeço et al., 2017; Dutrow and Henry, 2011; Büttner et al., 2016). Tourmaline may be used to interpret boron isotope geochemistry because it is the dominant boron-bearing phase in most crustal rocks (Palmer et al., 1992; Dyar et al., 2001; Dutrow and Henry, 2011; Xavier et al., 2008; Hazarika et al., 2015; Trumbull and Slack, 2018). Furthermore, boron may be associated with other rare elements and therefore can act as a proxy to trace ore mineralization (Tonarini et al., 1998, 2003; Jiang et al., 2002; Duchoslav et al., 2017).

The Dayishan ore field, Nanling Range (Fig. 1), is characterized by large-scale Sn-W polymetallic mineralization related to the Dayishan pluton (Zhou et al., 2005; He et al., 2011; Zeng et al., 2016; Sun et al., 2018). Tourmalines are widespread throughout the Dayishan ore field, and occur within granite, greisen and quartz veins. The petrogenesis of these tourmalines (e.g., morphology, species, elemental and boron geochemical feature) are poorly constrained. In addition, understanding the features of the genetic relationships between the tourmalines in the granite, greisen and quartz veins in this region provides insight into the mechanisms of granitic evolution, and for formulating exploration strategies of rare metal deposits.

Geological background

The South China Block (SCB) is composed of the Yangtze and Cathaysia Blocks, which merged during collisional tectonics in the Neoproterozoic (860 – 800 Ma), forming the Jiangnan orogenic belt (Fig. 1a; Zhao et al., 2011; Yao et al., 2016). The second stage of evolution was the formation of the Qin-Hang belt and intracontinental basins, and the final stage of activity was Triassic amalgamation during the Indosinian orogeny (Fig. 1; Yu et al., 2009; Zhou et al., 2018). Middle Jurassic subduction of the paleo-Pacific plate beneath the SCB resulted in extensive granitic magmatism and volcanism (Chen et al., 2008; Mao et al., 2013). From a spatial perspective, these granite plutons are controlled by faults and have complex genetic types (Wang et al., 2012; Mao et al., 2013; Cao et al., 2018a), which are associated with W-Sn-Nb-Ta polymetallic mineralization (Mao et al., 2008; Hua et al., 2010). In addition, most of these granitic plutons are tourmaline-bearing granites (e.g., Qitianling, Fanjingshan and Shangbao pluton, Guo et al., 2014; Yang et al., 2015b; Lu et al., 2020).

The Nanling W-Sn polymetallic province in South China, occupying an area of 170,000 km^2, has become one of China's nineteen principal metallogenic belts (Fig. 1b), containing > 83 and 63 percent of the total tungsten and tin reserves of China, respectively (Fig. 1c; Mao et al., 2007; Chen et al., 2016). The Dayishan ore field is situated in the northern margin of the middle section of Nanling metallogenic belt in the south China fold belt (Fig. 1). Devonian, Carboniferous, and Permian strata are widespread in the area and are mainly carbonates with few clastic rocks. (Fig. 2; Liu et al., 2005). The main structure inventory consists of folds and faults referred to as "faults of Dayishan trend" (Li et al., 2015). In the Dayishan pluton, the granitic rocks display a range of grain sizes with SiO_2 concentrations from 69.3 – 74.7 wt. % and $K_2O + Na_2O$ contents of 7.66 – 8.95 wt. % (Wu et al., 2005; Zhao et al., 2017). These granites are rich in volatile components (e.g., F, Cl and B) and metals (e.g., W, Sn and Bi), which are favorable for Sn mineralization (Zhao et al., 2017). Numbers of Sn, W, Cu, Pb, Zn, B deposits, hosted in the Dayishan ore field, show a clear distribution pattern which changes from Sn-W deposits (inner Dayishan pluton) to Cu-Pb-Zn-Sb-As-B deposits (edge of the Dayishan pluton) (Fig. 2; Zhang et al., 2014; Li et al., 2015; Sun et al., 2018).

Tourmaline occurrence and sample descriptions

The sample material for this study was collected from the northwestern part of the Dayishan pluton (Fig. 2). We have identified four types of tourmaline: (1) tourmaline in the coarse-grained monzogranite (Tur-G1) (Fig. 3a, b, c); (2) tourmaline in the medium–fine-grained monzogranite (Tur-G2) (Fig. 3a, d, f); (3) tourmaline aggregates associated with muscovite in greisen (Tur-Gr) (Fig. 4a, b); and (4) quartz vein tourmaline (Tur-V) (Fig. 5a, b). Characteristics of these tourmalines are summarized in Table 1 and described as follows.

Tourmaline in coarse-grained monzogranite (Tur-G1)

The coarse-grained monzogranite is pale gray, with a grain of 5 – 8 mm (Fig. 3a, b). The rock consists of quartz (30 – 35%), plagioclase (30%), alkali feldspar (30%) and biotite (10%) with accessory tourmaline, apatite, fluorite, and zircon (Fig. 3a, b, d, e). Tourmaline in coarse-grained monzogranite is intergranular and therefore difficult to identify in hand specimens (Fig. 3a, b), but thin section microscopy shows variable optical properties that allow the distinction of different varieties. Tourmaline is generally sub- to euhedral and is tens to hundreds of micrometers long. It often coexists with quartz and plagioclase as well as accessory minerals (e.g., zircon, fluorite and apatite) (Fig. 3d, e).

This is the peer-reviewed, final accepted version for American Mineralogist, published by the Mineralogical Society of America.
The published version is subject to change. Cite as Authors (Year) Title. American Mineralogist, in press.
DOI: https://doi.org/10.2138/am-2021-7591. http://www.minsocam.org/

Tourmaline shows a yellow-brownish absorption color, without obvious compositional zoning in BSE images.

Tourmaline in medium-fine grained monzogranite (Tur-G2)

The fresh medium-fine grained monzogranite is slightly dark grey (Fig. 2–3a) with grain sizes of 1 – 3mm. The major minerals of the rock are quartz (30-35%), alkali feldspar (30%), plagioclase (30%), biotite (about 10%), and the accessory minerals include tourmaline, zircon, fluorite and apatite (Fig. 3a, c, f, j, h). Tourmaline in the medium–fine-grained monzogranite (Tur-G2) forms needle- or short columnar crystals with 1 – 5mm in length (Fig. 3a, c). In thin section, tourmaline crystals are sub-euhedral to anhedral. Tourmaline crystals coexist with K-feldspar, plagioclase, quartz and minor accessory zircon (Fig. 3f, j, h, g, k), exhibit yellowish-brown color (Fig. 3f, g) and lack oscillatory zoning (Fig. 3g, k), similar to Tur-G1.

Tourmaline in greisen (Tur-Gr)

The greisen is gray to white and coarse-grained. The phenocrysts are mainly composed of quartz, muscovite, and tourmaline (Fig. 4a – d). Accessory minerals include pyrite and fluorite. Tourmaline in the greisen (Tur-Gr) occurs as large crystals (up to 15cm) and irregularly shaped aggregates (Fig. 4a, b), accounting for 20–30 vol% in monzogranite. In thin section, tourmaline usually has euhedral to subhedral shape and coexists with quartz, muscovite, pyrite and chalcopyrite (Fig. 4c, d, e). The tourmalines generally have yellow-brown cores (Tur-Gry) and blue rims (Tur-Grb), which (as shown in section 5) have distinct compositions (Fig. 4c, d, e, f).

Tourmaline in quartz vein (Tur-V)

Tourmaline in quartz veins exhibits elongated columnar shape or tourmaline aggregates (Fig. 5a, b). The Tur-V grains are blue and have no optical zoning (Fig. 5c, d). Although single tourmaline crystals are mostly less than 1 cm in length, the aggregates typically reach tens of centimeters in length and range from millimeters to centimeters in width. Tur-V also occurs as isolated grains with fluorite (Fig. 5c, d, e, f).

Analytical methods

Back-scattered electron (BSE) images

All samples were mounted in epoxy, polished and carbon coated to investigate growth zonation using a scanning electron microscope (SEM) prior to further analyses. Semiquantitative analyses and backscattered electron (BSE) images were collected on a Hitachi S-3600N scanning electron microscope fitted with a Bruker XFlash 5030 detector at the CAS Key Laboratory of Crust-Mantle Materials and Environments, University of Science and Technology of China (USTC), Hefei, China. Based on the SEM BSE imaging and energy dispersive spectrum (EDS) measurements, tourmalines were prepared for major and trace element and boron isotope analysis.

Electron microprobe analysis (EMPA)

The major and minor elements of tourmaline were quantified using the JEOL JXA-8530F Electron Probe Micro Analyzer at the Hefei Key Laboratory of Crust-Mantle Materials and Environments, University of Science and Technology of China. The analytical conditions were: accelerating voltage 15kV, beam current 20nA, and beam diameter 5μm. Data were later corrected on-line using a modified ZAF (atomic number, absorption, fluorescence) correction procedure. Peak counting time was 10s for Al, Na, Ca, Fe, Mg, Si and K, and 20s for Mn, Ti, F and Cl. Upper and lower background counting time was 5s for all elements. The following reference materials were used for instrument calibration: olivine for Si, pyrope garnet for Fe, Al, diopside for Ca, Mg, jadeite for Na, rhodonite for Mn, rutile for Ti, sanidine for K, and topaz for F. The relative uncertainty of a single oxide measurement is smaller than 1.5%. The detailed analytical procedures were similar to that described by Yang and Jiang (2012). The compositional formulae of tourmaline were calculated with the WinTcac program (Yavuz et al., 2013), based on fifteen cations (T + Z + Y) and thirty-one anions.

In-situ LA-MC-ICP-MS analysis

In-situ trace element analysis of tourmaline was performed by LA-ICP-MS at Beijing Createch Testing Technology Co., Ltd. The same grains were analyzed by both LA-ICP-MS and EPMA. Samples were inspected for mineral inclusions prior to analysis. Standards were NIST SRM 610, 612, USGS BIR-1G, BCR-2G and BHVO-2G. The above standards were analyzed after 10–15 unknowns. The analytical conditions contain the energy density of ~3J/cm^2, a spot beam diameter of 33μm together with a 10Hz repetition rate for 40s. The internal standard was ^{29}Si, as determined from electron microprobe analysis. The former USGS reference glasses were used for carrying out external calibrations. NIST glasses were adopted to correct signal drift. The ICPMSDataCal 12.0 software was used for performing raw data reduction offline (Liu et al., 2008).

The in-situ boron isotopic compositions of tourmaline were determined on thin polished sections by a Neptune Plus MC-ICP-MS and ESI-NWR213 laser-ablation system at the Beijing Createch Testing Technology Co., Ltd, Beijing, with a spot size of 80μm, repetition rate of 10Hz, and laser energy of 7 J/cm^2. ^{10}B and ^{11}B are received simultaneously statically with Faraday cups. The carrier gas was helium, which was mixed with argon prior to introduction into the mass spectrometer. Boron isotope standard tourmaline IAEA-B4 was used as the external standard (Tonarini et al., 2003), and IMR-RB1 was treated as the monitoring standard sample. The IMR RB1 standard yielded a mean $\delta^{11}B$ of -13.77 ± 0.13 (2σ), which is consistent with the values of -12.96‰ ± 0.97‰ (2σ) reported by Hou et al. (2010) within the limits of experimental error. Detailed description of the analytical methods can be found in Hou et al. (2010) and Yang and Jiang (2012).

Results

Major element compositions

Major element compositions of tourmaline samples are given in Table 2 and the complete database (n = 127) is deposited as supplementary Table A. Tourmalines in monzogranite (Tur-G1 and Tur-G1) display the same major element contents with high concentrations of SiO_2 (31.87 – 34.71 wt. %), Al_2O_3 (31.61 – 33.82 wt. %), TiO_2 (0.12 – 0.76 wt. %), FeO (12.29 – 14.91 wt. %) and low contents of MnO (0.14 – 0.53 wt. %), MgO (1.27 – 4.28 wt. %), CaO (0.04 – 0.41 wt. %), Na_2O (1.47 – 2.26 wt. %), K_2O (< 0.1 wt. %) and F (< 0.27 wt. %) (Fig. 6, 7). In addition, tourmalines in greisen (Tur-Gry and Tur-Grb) also show high contents of SiO_2 (33.90 – 35.81 wt. %), Al_2O_3 (30.06 – 34.05 wt. %), TiO_2 (0.01 – 0.94 wt. %), FeO (12.38 – 17.36 wt. %) and low contents of MnO (0.06 – 0.51 wt. %), MgO (0.03 – 0.51wt. %), CaO (0.02 – 0.30 wt. %), Na_2O (1.45 – 2.22 wt. %), K_2O (< 0.1 wt. %) and F (< 0.1 wt. %) (Fig. 6, 7). Compared with compositions of tourmaline in the monzogranites, Tur-Grb have higher FeO contents and lower MgO and TiO_2 (Fig. 7a, b). Major elements of tourmalines from quartz-vein (Tur-V) show similar contents of SiO_2, MnO, Na_2O, K_2O and F with other types of tourmalines, but Tur-V has low TiO_2 (0.00 – 0.27 wt. %), MgO (0.01 – 0.23 wt. %) and FeO (13.67 – 16.79 wt. %) contents.

The formula of tourmaline is expressed as $XY_3Z_6(T_6O_{18})(BO_3)_3V_3W$, where X = Ca^{2+}, Na^+, K^+, X□ (vacancy); Y = Mg^{2+}, Fe^{2+}, Mn^{2+}, Al^{3+}, Ti^{4+}; Z = Mg^{2+}, Al^{3+}, Fe^{3+}, Cr^{3+}, V^{3+}; T = Si^{4+}, Al^{3+}, (B^{3+}); V = OH^-, O^{2-}; and W = OH^-, F^-, O^{2-}. According to compositional variations, the tourmaline series are mainly divided into 'three groups' and listed in supplementary Table B (Hawthorne and Dirlam, 2011). On the grounds of X-site occupancy calculated by Henry et al. (1996, 2011), nearly all of our tourmaline samples are alkali group tourmalines (Fig. 6a), and data of all tourmalines show narrow variation and are plotted in schorl field and the field of Li-poor granite (Fig. 6b, c). Moreover, all tourmalines are Fe-rich with a slight variation in Fe / (Fe + Mg) ratios (0.62 and 1.00) and Na/(Na + Ca) ratios (0.93 and 1.00). On the ^{x}(□/(□ + Na)) vs. Fe/(Fe + Mg) and ^{x}(Ca/(Ca + Na)) vs. Mg/(Mg + Fe) diagrams (Fig. 7a, b), data of all tourmalines belong to the schorl series.

The tourmaline composition can be expressed as component exchange vectors (Henry and Dutro 1990, 2012; Henry et al., 2011). In the Mg-Fe plot (Fig. 7c, d), tourmalines in granite and greisen exhibit a linear relationship, having a negative slope of 1:1. This means that $MgFe_{-1}$ function is the primary substitution vector, while Tur-V could relate to the $FeAl_{-1}$ vector (Fig. 7c, d). The (R^{2+}+X_{vac}) vs. (Al-X_{vac}) figure displays a negative relationship between Tur-Gr and Tur-V (Fig. 7e), which can be attributed to the low concentrations of Al possibly from the exchange of $FeAl_{-1}$.

Trace elements

Table 3 lists the range and average trace element contents, and supplementary Table C provides the complete database (n = 55). Most elements show very low concentrations (always < 10 ppm), occasionally below detection limit, such as W (0 – 0.16), Pb (1.02 – 4.91), Cu (0.00 – 5.72). Higher concentrations were observed for Li (140 – 487 ppm), Sc (0.00 – 65.98 ppm), Zn (376 – 742 ppm), La (0.16 – 6.75 ppm), Ce (0.25 – 16.83 ppm) and Sn (115 – 485 ppm). The Tur-V and Tur-Grb show significantly higher contents of Sn and Zn (average = 285 and 607, respectively) than Tur-G1, Tur-G2 and Tur-Grb (average = 136 and 408, respectively).

All types of tourmaline display compositional variations, but they mainly show low total REE abundances ranging from 0.94 to 31.30 ppm. Tourmalines in monzogranite have the highest LREE and the lowest HREE compared to other types of tourmaline. In addition, Tur-G1 and Tur-Gry tourmaline show the negative Eu anomalies (Fig. 8a, c). However, the Tur-Grb and Tur-V show positive Eu anomalies (Fig. 8c, d), and all have a concave upward pattern with low amounts at Ho, which gradually increases towards Lu. In the primitive mantle-normalized spider diagram (Fig. 8b, c, d), there are no remarkably enriched or depleted large ion lithophile elements (LILE), and high field strength elements (HFSE) show positive Ti anomalies, negative Ba, Sr and Y anomalies. Element variation diagrams are shown in Fig. 9, and there is no obvious correlation between these trace elements.

Boron isotopes

Boron possesses two stable isotopes ^{11}B amounting to 80.1% and ^{10}B making up the remaining 19.9% (Barth, 1993). Boron isotopic data of tourmalines are summarized in Table 4 and further plotted in Fig. 10. Tourmalines in the monzogranite (Tur-G1, Tur-G2 and Tur-Gry) have a limited variation of

$\delta^{11}B$ values varying from -15.58 ‰ to -14.09 ‰ (mean = -14.88 ‰, n = 47). However, Tur-Grb and Tur-V show slightly lower boron isotope values ranging from -16.15 ‰ to -14.91 ‰ (mean = -15.65 ‰, n = 13) and –16.31 ‰ to -15.42 ‰ (mean = -15.81 ‰, n = 13), respectively. There is no clear $\delta^{11}B$ variation between the core and rim of Tur-G1, Tur-G2 and Tur-V (Fig. 3i, e; Table 4).

Discussion

Formation of tourmaline

Tourmaline in the monzogranite (Tur-G1 and Tur-G2) is in textural equilibrium with other phases (e.g., quartz and feldspar) with planar or arc-shaped contacts, and there are no structural evidence that they have replaced pre-existing phases, indicating that it was contemporaneous with the crystallization of the magma (Fig. 3d − h). In addition, all tourmaline samples in the granite are plotted in the field of Li-poor granite (Fig. 6b, c), and the $\delta^{11}B$ values of tourmalines in the monzogranite exhibit a narrow range between -15.55 ‰ and -14.09 ‰ (Table 4; Fig. 10a), which is significantly different from those occurring in sedimentary rocks, marine carbonates or Non-marine evaporites (Fig. 10b, Smith and Yardley, 1996; Marschall and Jiang, 2011;), but relatively consistent with those in the magmatic rocks (e.g., Xavier et al., 2008; Yang et al., 2015b). Therefore, Tur-G1 and Tur-G2 are most likely crystallized from the boron-rich silicate melt.

Geisenization is the result of metasomatic alteration of granites (Fig. 4). The cores of tourmaline in greisen (Tur-Gry) are yellow-brown, subhedral to anhedral, and display similar optical features with Tur-G1 and Tur-G2. Geochemically, the Tur-Gry tourmalines exhibit high Fe/(Fe + Mg) and Ca/(Ca + Na) ratios and display chemical features related to Li-poor granites (Fig. 6c, d, 7a, b) and share comparable REE patterns with tourmalines in the monzogranite. In addition, the $\delta^{11}B$ values of Tur-Gry are in the narrow range of -15.58 ‰ to -14.43 ‰, which is also similar to the Tur-G1 and Tur-G2 (Fig.10a), thus implying the possibility that Tur-Gry tourmalines were preserved from the magmatic stage. In contrast to the yellow-brown tourmaline, blue tourmalines in Tur-V and Tur-Grb are distinct in composition, paragenesis (coexisting with quartz ± muscovite), have higher Fe/(Fe+Mg) ratios, higher Zn and Sn contents, and lower $\delta^{11}B$ ratios. Thus, the contrasting chemical compositions (Fig. 9) and mode of occurrence of Tur-V indicate the likelihood that they were precipitated from the hydrothermal fluid (e.g., Jiang, 1999; Trumbull et al., 2011). By analogy, similarities of Tur-V and Tur-Grb indicate that the latter are hydrothermal in origin (Fig. 8). According to the above discussion, we can summarize that Tur-G1, Tur-G2 and Tur-Gry formed from the granitic melt, while Tur-Grb and Tur-V precipitated from hydrothermal fluids.

Chemical variations in magmatic and hydrothermal tourmaline

The tourmaline in the Dayishan monzogranite belongs to the schorl series, and primary substitution vector of Dayishan tourmaline is $MgFe_{-1}$ function (Fig. 7), which is consistent with evolution of the magmatic tourmaline, indicating that the crystallization sequence of tourmaline (Tur-G1 and Tur-G2) is consistent with the expected changes in composition during the fractionation of boron-rich magmas. Moreover, in general, in boron-rich granitic systems, magmatic tourmaline is Fe enriched, while the hydrothermal tourmaline is Mg enriched (e.g., Duchoslav et al., 2017; van Hinsberg et al., 2011; Yang et al., 2015b). However, the increase of Fe content in Dayishan hydrothermal tourmaline (Fig. 7a, b) may be due to the addition of exogenous substances. In addition, the sharp changes of trace elements such as Sr, Sn, Nd, Ta, Cu, Pb and Zn in the hydrothermal tourmaline also

This is the peer-reviewed, final accepted version for American Mineralogist, published by the Mineralogical Society of America.
The published version is subject to change. Cite as Authors (Year) Title. American Mineralogist, in press.
DOI: https://doi.org/10.2138/am-2021-7591. http://www.minsocam.org/

reflect the influence of external fluid (Fig. 10). There may be two causes for the increase of element content in hydrothermal tourmaline: one is that when silicate minerals break down, they release elements from granite that can be added to tourmaline during crystallization; the second is the extraction of these elements by external fluids (such as deep-circulated meteoric water and metamorphic fluid) through water-rock interactions (Zhou et al., 2019; Zhao et al., 2019; Hu et al., 2020). However, in the former case, these elements should increase sharply in all hydrothermal tourmalines, while the content variation of these elements is not evident in Tur-Grb, but significantly increases in Tur-V. Therefore, we consider the second case is more likely. In addition, the content of Sr increases dramatically in late hydrothermal stage. Similarly, Duan et al. (2019) and Zhao et al. (2019) also suggested the higher Sr contents in the vein tourmalines is the result of compositional contribution from the surrounding strata. Combined with the previous analysis (Yang et al., 2015; Zhao et al., 2019), it can be concluded that Sr in the strata may be brought into hydrothermal system by meteoric water, resulting in a sharp increase of Sr in late hydrothermal stage. The fact that Pb is very active in the fluid and its almost the highest mobility (Kogiso et al., 1997) make it easy to transfer from the strata to the fluid, and the same explanation applies to Zinc. Moreover, the Nb and Ta are more likely to remain in melt rather than in fluid (Borodulin et al., 2009). Nevertheless, there is an increase of Nb and Ta from magmatic tourmalines to hydrothermal tourmalines, further indicating the involvement of external materials.

There are different REE patterns between magmatic and hydrothermal tourmalines (Fig. 8); for example, magmatic tourmalines show flat HREE-patterns with negative Eu anomalies, while hydrothermal tourmalines exhibit concave upward-shaped REE pattern with positive Eu anomalies. Experimental studies show that tourmaline has a preference for Eu^{2+} over Eu^{3+} (van Hinsberg, 2011a), indicating that the negative Eu anomalies in the earlier tourmalines is due to the preferential incorporation of Eu^{2+} in co-genetic plagioclase. Hence, Tur-G1, Tur-G2 and Tur-Gry type tourmalines with significantly negative Eu anomaly probably crystallized directly from the magma. The Eu anomalies in the later hydrothermal tourmalines (Tur-Grb and Tur-V) exhibit obviously positive characteristic. The ∑REE content of hydrothermal tourmalines is lower than that of magmatic tourmalines, possibly due to the crystallization of accessory minerals (e.g., apatite and zircon) (Yang et. al., 2015). Thus, the positive Eu anomalies in the hydrothermal tourmalines (Tur-Grb and Tur-V) may be a simple indication of differing partition coefficients that the tourmaline prefers Eu^{2+}, but not the REE^{3+}.

In addition, several possible mechanisms can explain the concave upward-shaped REE patterns: (1) accessory minerals affect the REE patterns in tourmaline during analysis; (2) early crystallization of minerals (e.g., amphibole and xenotime) during hydrothermal fluid evolution; (3) REE-fluoride complexes lead to HREE enrichments. Firstly, most elements show very low concentrations (especially Zr, Y, Th, U, and Y < 3 ppm), indicating negligible influence of accessory mineral inclusions (zircon, apatite, monazite, and allanite) on the REE patterns of tourmaline. Secondly, the precipitation of amphibole and xenotime, which have preference for MREE, may lead to the concave downward-shaped REE patterns of tourmalines (e.g., Jiang et al., 1997; Aleinikoff et al., 2012a, 2012b). However, the amphibole and xenotime are not detected in the hydrothermal veins we studied, and hydrothermal tourmalines have the same MREE contents as magmatic tourmalines. Therefore, the second mechanism above can be precluded. Hydrothermal tourmalines, possessing similar REE patterns as our samples, have also been identified in the Qitianling pluton (Yang et al., 2015b) and the Mopanshan pluton (Duan et al., 2019). These authors suggested that the HREE enrichment in tourmalines may be caused by REE-fluorite complexes for the reason that the HREE are more strongly complexed than the LREE under geologically reasonable ligand concentrations (Wood, 1990). As the fluorite exists in the quartz veins, REE-fluorite complexes may exist in the fluid during the precipitation of hydrothermal tourmalines. Consequently, hydrothermal tourmalines in Dayishan exhibit concave upward-shaped REE patterns.

If tourmaline is a passive geochemical monitor, then it has significance in the interpretation of geological processes and mineral exploration. Some authors questioned the passive character of tourmaline because its trace-element variations typically possess covariant relationship, e.g., V vs. Sc, Sn vs. Sr. (Yang et al., 2015b; Duchoslav et al., 2017), but these correlations are not found in Dayisham tourmalines. In addition, this can be distinguished from the diagram of trace elements versus Fe/(Fe +Mg) (e.g. Marks et al., 2013; Yang et al., 2015b), because if the absorption of trace elements in tourmaline were largely controlled by its main element composition, the slope of all tourmalines would be the same. In this study, no correlation between elements and Fe/(Fe + Mg) ratio was observed (Fig. 9j – o), which further indicate the passive character of tourmaline.

Boron source and variations

Tourmaline $\delta^{11}B$ values are mostly affected by sources of boron (Palmer and Slack, 1989). The boron isotopic compositional variations (Fig. 10b) in the magmatic tourmalines (−15.58 ‰ to −14.09 ‰; mean = −14.90 ‰) from Dayishan are close to the boron isotopic values of other granites in SCB (Fig. 10b), and slightly lighter than the continental crust composition (−10 ± 3‰; Fig. 10b; van Hinsberg et al., 2011). In addition, there are no remarkable boron isotopic compositional variations among the tourmaline (Tur-G1 and Tur-G2) cores and rims, suggesting that magmatic tourmalines

(Tur-G1 and Tur-G2) had a single source of boron. Besides, at magma temperature, boron isotopic fractionation between melt and tourmaline is relatively small (~700 °C; Δ Tur-melt = ~1.0‰; Palmer et al., 1992; Tonarini et al., 1998; Meyer et al., 2008), but with cooling and crystallization, the fractionation becomes larger. Therefore, Tur-G1 and Tur-G2 should crystallize at the same temperature, and the composition of $\delta^{11}B$ of Dayishan melts may be at -15 ‰ considering the average $\delta^{11}B$ value recorded by magmatic tourmalines.

However, hydrothermal tourmalines show slightly lighter B isotopic values (−16.31 ‰ to −14.91 ‰; mean = −15.73 ‰) than magmatic tourmalines (Fig. 10a). The difference in boron isotopic values between tourmalines can be explained by the hydrothermal fluid exsolution from the melt, B isotopic fractionation or different boron sources (Trumbull et al., 2008, 2013; Marschall et al., 2009; Drivenes et al., 2015; Zhang et al., 2018; Duan et al., 2019; Qiao et al., 2019; Zhao et al., 2019; Zhen et al., 2019; Li et al., 2020). For the first model, the experimental results of natural samples showed that the exsolved fluid and tourmaline crystallized from it would be isotopically heavier than the primary magma (Jiang and Palmer, 1997; Hervig et al., 2002; Kowalski and Wunder, 2018; Zhao et al., 2019). Hence, we can exclude this possibility.

Rayleigh fractionation is capable of generating difference in $\delta^{11}B$ values (e.g., Trumbull et al., 2008; Pal et al., 2010; Duan et al., 2019). In this study, with the continuous growth of tourmaline and consumption of liquid as well as the progressive decrease of temperature, the isotopic composition of boron in tourmaline gradually becomes heavier (Fig. 11). All boron compositions observed in hydrothermal tourmaline of Dayishan are significantly low. Therefore, this model is unlikely. Although this model may be true if the temperature is decreased during crystallization and fractionation, the late addition of an isotopically lighter fluid in the late stage of greisen formation may be a more valid explanation for the lighter $\delta^{11}B$ composition. Here we offer two lines of isotope and chemical evidence. First, the high Sn, Zn, Sr contents of hydrothermal tourmaline and positive Eu anomalies indicate the presence of external materials. Second, the external hydrothermal fluid must be isotopically lighter. To achieve the $\delta^{11}B$ of about -15‰ in the mixed fluid, the fluid may have been in the range of -16/-17‰, depending upon the ratio of mixing. At 650 °C this -15‰ mixed fluid would yield a tourmaline composition of $\delta^{11}B$ ~ -16, which then would develop to heavier values during cooling and fractionation. That would explain the isotope data in the blue rims and the veins.

Implications for the mineralization

Tin-tungsten mineralization is generally associated with low fO_2 magmas, whereas Cu-Au mineralization is associated with high fO_2 magmas (Sun et al., 2013, 2015; Zhang et al., 2017). All tourmalines in Dayishan are characterized by an Fe^{2+}, schorl-rich component, suggesting crystallization in relatively reducing environment (Trumbull et al., 2011), which promoted the enrichment of Sn (Duchoslav et al., 2017). Additionally, the presence of tourmaline and fluorite indicates the existence of B, F-rich melt/fluid in the Dayishan ore field, which is also in favor of the Sn mineralization (e.g., Myint et al., 2018).

Tourmaline has been widely employed to predict and explore new mineral deposits. According to previous tourmaline studies in Nanling Range (Jiang et al., 1999; Yang et al., 2015b), tourmalines related to Sn deposit have high contents of Sn: for instance, tourmalines originating from the Dachang Sn-W deposit located in Guangxi, Nanling Range, have a concentration of Sn at 513 ppm (Jiang et al., 1999); tourmalines from Sn deposits linked to Qitianling pluton have a high Sn content of 227 to 1792 ppm (Yang et al., 2015b); however, tourmaline from barren granites show low Sn contents, mostly < 50 ppm (e.g., Audétat et al., 2008; Hong et al., 2017; Trumbull et al., 2018). Thus, the characteristic of high Sn content of tourmaline has potential as an exploration tool.

A number of Sn, Zn deposits have been explored in Dayishan, such as Shimaochong Sn, Maozaishan Sn and Wanjinwo Pb-Zn-Sn deposits (Li et al., 2000; Liu et al., 2002; Zhao et al., 2017; Sun et al., 2018). Some deposits are close to the pluton margin and veins transect this margin. Other deposits may be located close to the pluton roof (that is where greisens commonly form; Fig. 2). Based on our results, the high concentrations of Sn and Zn that characterize the hydrothermal tourmalines (up to 485 ppm and 487 ppm, respectively) indicate the existence of Sn- and Zn-rich fluids in the Dayishan ore field. The lighter ^{11}B values of hydrothermal tourmalines reveal that metals (Sn and Zn) may not come from the granite, but from the host rock, and are mobilized by the heat of the contact metamorphism.

Acknowledgments

This study was supported by the National Natural Science Foundation of China (42030801, 41803038), China Geological Survey (DD20190154) and Guangxi Natural Science Foundation (2018GXNSFAA138193). We are grateful to Jianfeng Li and Qidi Yang for guiding in the field. Ruixia Bai and Jin Tan are thanked for their assistance with EMPA. Dewei Kong is thanked for his assistance during LA-MC-ICP-MS trace elements and boron isotopic analysis.

Reference

Aleinikoff JN, Hayes, TS, Evans KV, Mazdab FK, Pillers RM, Fanning CM (2012a) SHRIMP U–Pb ages of xenotime and monazite from the Spar Lake red bed-associated Cu–Ag deposit, western Montana: implications for ore genesis. Econ Geol 107: 1251–1274

Aleinikoff JN, Slack JF, Lund K, Evans KV, Fanning CM, Mazdab FK, Wooden JL, Pillers RM (2012b) Constraints on the timing of Co–Cu±Au mineralization in the Blackbird district, Idaho, using SHRIMP U-Pb ages of monazite and xenotime plus zircon ages of related mesoproterozoic orthogneisses and metasedimentary rocks. Econ Geol 107: 1143–1175.

Audétat A, Pettke T, Heinrich CA, Bodnar RJ (2008) The composition of magmatic–hydrothermal fluids in barren and mineralized intrusions. Econ Geol 103: 877–908.

Barth S (1993) Boron isotope variations in nature: a synthesis. Geol Rundsch 82: 640–651.

Barton MD (2014) Iron oxide (−Cu–Au–REE–P–Ag–U–Co) systems. In: Scott SD Geochemistry of mineral deposits. Treatise on Geochem 13: 515–541.

Borchert M, Wilke M, Schmidt C, Cauzid J, Tucoulou R (2010) Rb and Sr partitioning between haplogranitic melts and aqueous solutions. Geochim Cosmochim Acta 74: 1057–1076.

Borodulin GP, Chevychelov VY, Zaraysky GP (2009) Experimental study of partitioning of tantalum, niobium, manganese, and fluorine between aqueous fluoride fluid and granitic and alkaline melts. Dokl. Earth Sci 427: 868–873.

Büttner SH, Reid W, Glodny J, Wiedenbeck M, huwa G, Moloto T, Gucsik A (2016) Fluid sources in the Twangiza-Namoya gold belt (Democratic epublic of Congo): evidence from tourmaline and fluid compositions, and from boron and Rb–Sr isotope systematics. Prec Res 280:161–178.

Cao JY, Wu QH, Yang XY, Kong H, Li H, Xi XS, Huang QH, Liu B (2018a) Geochronology and Genesis of the Xitian W–Sn Polymetallic Deposit in Eastern Hunan Province, South China: Evidence from Zircon U–Pb and Muscovite Ar–Ar Dating, petrochemistry, and Wolframite Sr–

Nd–Pb Isotopes. Minerals 8: 111.

Cao JY, Yang XY, Du JG, Wu QH, Kong H, Li H, Wan Q, Xi XS, Gong YS, Zhao HR (2018b) Formation and geodynamic implication of the Early Yanshanian granites associated with W–Sn mineralization in the Nanling range, South China: an overview. Int Geol Rev 60: 1744–1771.

Chaussidon M, Albarède F (1992) Secular boron isotope variations in the continental crust: an ion microprobe study. Earth Planet Sci Lett 108: 229–241.

Che XD, Wang RC, Wu FY, Zhu ZY, Zhang WL, Hu H, Xie L, Lu JJ, Zhang D (2019) Episodic Nb–Ta mineralisation in South China: Constraints from in situ LA–ICP–MS columbite-tantalite U–Pb dating. Ore Geol Rev 105: 71–85.

Chen C, Lee C, Shinjo R (2008) Was there Jurassic paleo-Pacific subduction in South China? Constraints from $^{40}Ar/^{39}Ar$ dating, elemental and Sr–Nd–Pb isotopic geochemistry of the Mesozoic basalts. Lithos 106: 83–92.

Chen YX, Li H, Sun WD, Ireland T, Tian XF, Hu YB, Yang WB, Chen C, Xu DR (2016) Generation of Late Meosozic Qianlishan A2-type granite in Nanling Range, South China: Implications for Shizhuyuan W–Sn mineralization and tectonic evolution. Lithos 266–267: 435–452.

Codco MS, Weis P, Trumbull RB, Pinto F, Lecumberri SP, Franziska DH (2017) Chemical and boron isotopic composition of hydrothermal tourmaline from the Panasqueira W-Sn-Cu deposit, Portugal. Chem. Geol. 468: 1–16

Drivenes K, Larsen RB, Müller A, Sørensen BE, Wiedenbeck M, Raanes M (2015) Late-magmatic immiscibility during batholith formation: assessment of B isotopes and trace elements in tourmaline from the Land's End granite, SW England. Contrib Mineral Petrol 169: 1–27.

Duan ZP, Jiang SY, Su HM, Zhu XY (2019) Tourmaline as a recorder of contrasting boron source and potential tin mineralization in the Mopanshan pluton from Inner Mongolia, northeastern China. Lithos 354: 205–224.

Duchoslav, M, Marks MAW, Drost K, Mccammon C, Marschall HR, Wenzel, T, Markl, G (2017) Changes in tourmaline composition during magmatic and hydrothermal processes leading to tin-ore deposition: the Cornubian Batholith, SW England. Ore Geol Rev 83: 215–234.

Dutrow BL, Henry DJ (2011) Tourmaline: a geologic DVD. Elements 7: 301–306.

Dutrow BL, Henry DJ (2018) Tourmaline compositions and textures: reflections of the fluid phase. J. Geosci 63: 99–110.

Dyar MD, Wiedenbeck M, Robertson, D, Cross LR, Delaney JS, Ferguson K, Francis CA, Grew ES, Guidotti CV, Hervig, RL, Hughes, JM, Husler, J, Leeman, W, McGuire, AV, Rhede, D, Rothe, H, Paul, RL, Richards, I, Yates, M (2001) Reference minerals for the microanalysis of light elements. Geostand Newsl 25: 441–463.

Guo HF, Xia XP, Wei, GJ, Wang, Q, Zhao, ZH, Huang, XL, Zhang, HY, Yuan C, Li WX (2014) LA-MC-ICPMS in-situ boron isotope analyses of tourmalines from the Shangbao granites (southern Hunan Province) and its geological significance. Geochimica 43: 11–19.

Hawthorne FC, Dirlam DM (2011) Tourmaline the indicator mineral: from atomic arrangement to Viking navigation. Elements 7: 307 – 312.

Hazarika P, Mishra, B, Pruseth, KL (2015) Diverse tourmaline compositions from orogenic gold deposits in the Hutti-Maski Greenstone Belt, India: implications for sources of ore-forming fluids. Econ Geol 110: 337–353.

He, WH (2011) Metallogenic Model of Tin Polymetallic Deposits of Dayishan Area,Hunan Province. Geology and Mineral Resources of South China 27: 14–21 (in Chinese with English abstract).

Henry DJ, Guidotti CV (1985) Tourmaline as a petrogenetic indicator mineral: an example from the staurolite grade metapelites of NW Maine. Am Mineral 70: 1–15.

Henry DJ, Dutrow BL (1990) Ca substitution in Li-poor aluminous tourmaline. Can Mineral 28: 101–114.

Henry DJ, Dutrow BL (1996) Metamorphic tourmaline and its petrologic applications. Rev Mineralogy 33: 503–557.

Henry DJ, Dutrow BL (2012) Tourmaline at diagenetic to low-grade metamorphic conditions: its petrologic applicability. Lithos 154: 16–32.

Henry DJ, Novák M, Hawthorne FC, Ertl A, Dutrow BL, Uher P, Pezzotta F (2011) Nomenclature of the tourmaline-super group minerals. Am Mineral 96: 895–913.

Hervig RL, Moore GM, Williams LB, Peacock SM, Holloway JR, Roggensack K, 2002. Isotopic and elemental partitioning of boron between hydrous fluid and silicate melt. Am Mineral 87: 769–774.

Hou KJ, Li YH, Xiao YK, Liu F, Tian YR (2010) In situ boron isotope measurements of natural geological materials by LA–MC–ICP–MS. Chin. Sci. Bull 55: 3305–3311 (in Chinese with English abstract).

Hong W, Cooke DR, Zhang L, Fox N, Thompson J (2017) Tourmaline-rich features in the Heemskirk and Pieman Heads granites from western Tasmania, Australia: Characteristics, origins, and implications for tin mineralization. Am. Mineral. 102: 876–899.

Hua RM, Li GL, Zhang WL, Hu DL, Chen PR, Chen WF, Wang XD (2010) A tentative discussion on differences between large-scale tungsten and tin mineralizations in South China. Miner Deposita 29: 9–23.

Iveson AA, Webster JD, Rowe MC, Neill OK (2016) Magmatic–hydrothermal fluids and volatile metals in the Spirit Lake pluton and Margaret Cu–Mo porphyry system, SW Washington, USA. Contrib Mineral Petrol 171: 20–31.

Jiang SY, Han F, Shen JZ, Palmer MR (1999) Chemical and Rb–Sr, Sm–Nd isotopic systematics of tourmaline from the Dachang Sn-polymetallic ore deposit, Guangxi Province, P.R. China. Chem Geol 157: 49–67.

Jiang SY, Palmer MR, Peng QM, Yang JH (1997) Chemical and stable isotopic compositions of Proterozoic metamorphosed evaporites and associated tourmalines from the Houxianyu borate deposit, eastern Liaoning, China. Chem Geol 135: 189–211.

Jiang SY, Palmer MR, Yeats C (2002) Chemical and boron isotope compositions of tourmaline from the Archean Big Bell and Mount Gibson gold deposits, Murchison Province, Yilgarn Craton, Western Australia. Chem Geol 188: 229–247.

Jiang SY, Yu JM, Lu JJ (2004) Trace and rare earth element geochemistry in tourmaline from the Yunlong tin deposit, Yunnan, China: implication for magmatic-hydrothermal fluid evolution and ore genesis. Chem Geol 209: 193–213.

Kalliomaki H, Wagner T, Fusswinkel T, Sakellaris G (2017) Major and trace element geochemistry of tourmalines from Archean orogenic gold deposits: proxies for the origin of gold mineralizing fluids? Ore Geol. Rev. 91: 906–927.

Kogiso T, Tatsumi Y, Nakano S (1997) Trace element transport during dehydration processes in the subducted oceanic crust: Experiments implications for the origin of ocean island basalts. Earth Planet. Sci. Lett 148: 193–205.

Kowalski PM, Wunder B (2018) Boron isotope fractionation among vapor-liquids-solids-melts: experiments and atomistic modeling. In: Marschall, H, Foster, G. (Eds.), Boron Isotopes-the Fifth

Element. Springer International Publishing, pp 33–69.

Kowalski PM, Wunder B, Jahn S (2013) Ab initio prediction of equilibrium boron isotope fractionation between minerals and aqueous fluids at high P and T. Geochim Cosmochim Acta 101: 285–301.

Longfellow KM, Swanson SE (2011) Skeletal tourmaline, undercooling, and crystallization history of the Stone Mountain granite, Georgia, USA. Can Mineral 49: 341–357.

Li JX, Fan WM, Zhang LY, Ding L, Yue YH, Xie J, Cai F, Sein K, Y (2020) B-rich melt immiscibility in Late Cretaceous Nattaung granite, Myanmar: Implication by composition and B isotope in tourmaline. Lithos 356–357: 1–12.

Li HC (2000) The prospecting significance of tourmalinization and grenization in Dayishan granite body. Hunan Geology 19: 233–236 (in Chinese with English abstract).

Li Y, Zhang YQ, Su JB, Li JH, Dong SW (2015) Zircon U-Pb dating of Dayishan and Tashan Plutons in Hunan Province and its tectonic implications. Act Geosci Sin: 303–312 (in Chinese with English abstract).

Liu TS (2002) Geological characteristics and genesis of rock body-type tin deposits in the Dayishan ore field. Geology in China 29: 411–415 (in Chinese with English abstract).

Liu YR, Kuang J, Ma Q, Bo DY (2005) ^{40}Ar–^{39}Ar dating of biotite in south Dayishan granite and Its geological significance. Resources Survey and Environment 26： 244–249 (in Chinese with English abstract).

Liu YS. Hu ZC, Gao S (2008) In situ analysis of major and trace elements of anhydrous minerals by LA-ICP-MS without applying an internal standard. Chem Geol 257: 34–43.

Lu X, Wang RC, Romer RL, Che XD, Hu Huang, Xie L, Tian EN (2020) Neoproterozoic Nb-Ta-W-Sn bearing tourmaline leucogranite in the western part of Jiangnan Orogen: Implications for episodic mineralization in South China. Lithos. 360 – 361: 1 – 15.

Mao JW, Cheng YB, Chen MH, Pirajno F (2013) Major types and time-space distribution of Mesozoic ore deposits in South China and their geodynamic settings. Miner. Deposita 48: 267–294.

Mao JW, Xie GQ, Gu, CL, Chen YC (2007) Large scale tungsten-tin mineralization in the Nanling region, South China: Metallogenic ages and corresponding geodynamic processes: Act Petrolo Sin 23: 2329–2338 (In Chinese with English abstract).

Mao JW, Xie GQ, Guo CL, Yuan SD, Cheng YB, Chen YC (2008) Spatial-temporal distribution of Mesozoic ore deposits in south China and their metallogenic settings. Geol J China Univ 14: 510–526 (In Chinese with English abstract).

Marks MAW, Marschall HR, Schühle, P, Guth, A, Wenzel, T, Jacob, D.E, Barth, M, Markl, G (2013) Trace element systematics of tourmaline in pegmatitic and hydrothermal systems from the Variscan Schwarzwald (Germany): the importance of major element composition, sector zoning, and fluid or melt composition. Chem Geol 344: 73–90.

Marschall HR, Meyer C, Wunder B, Ludwig T, Heinrich W (2009) Experimental boron isotope fractionation between tourmaline and fluid: confirmation from in situ analyses by secondary ion mass spectrometry and from Rayleigh fractionation modelling. Contrib Mineral Petrol 158: 675–681.

Marschall HR, Jiang SY (2011) Tourmaline isotopes: no element left behind. Elements 7: 313–319.

Meyer C, Wunder B, Meixner A, Romer R.L, Heinrich W (2008) Boron-isotope fractionation between tourmaline and fluid: an experimental re-investigation. Contrib Mineral Petrol 156: 259–267.

Myint AZ, Yonezu K, Boyce AJ, Selby D, Scherstén A, Tindell T, Watanabe K, Swe YM (2018) Stable isotope and geochronological study of the Mawchi Sn-W deposit, Myanmar: Implications for timing of mineralization and ore genesis. Ore Geol Rev 95: 663–679.

Pal DC, Trumbull RB, Wiedenbeck M (2010) Chemical and boron isotope compositions of tourmaline from the Jaduguda U-(-Cu-Fe) deposit, Singhbhum shear zone, India: implications for the sources and evolution of mineralizing fluids. Chem Geol 277: 250–260.

Palmer MR, London D, Morgan GB, Babb HA (1992) Experimental determination of fractionation of $^{11}B/^{10}B$ between tourmaline and aqueous vapor: a temperature and pressure-dependent isotopic system. Chem Geol 101: 123–129.

Palmer MR, Slack JF (1989) Boron isotopic composition of tourmaline from massive sulfide deposits and tourmalines. Contrib Mineral Petrol 103: 434–451.

Qiao XY, Li WB, Zhang LJ, White NC, Zhang FH, Yao ZW (2019) Chemical and boron isotope compositions of tourmaline in the Hadamiao porphyry gold deposit, Inner Mongolia, China. Chem Geol 519: 39–55.

Slack JF, Palmer MR, Stevens BPJ, Barnes RG (1993) Origin and significance of tourmaline-rich rocks in the Broken Hill district, Australia. Econ Geol 88:505–541.

Slack JF, Trumbull RB (2011) Tourmaline as a recorder of ore-forming processes. Elements 7: 321–326.

Sun HR, Zhao Z, Yan GS, Lu ZC, Huang ZL, Yu XF (2018) Geological and geochronological constraints on the formation of the Jurassic Maozaishan Sn deposit, Dayishan orefield, South China. Ore Geol Rev 94: 212-224.

Sun T (2006) A new map showing the distribution of granites in South China and its explanatory notes. Geological Bulletin of China 25: 332–335 (in Chinese with English abstract).

Sun W, Huang R, Li H, Hu Y, Zhang C, Sun S, Zhang L, Ding X, Li C, Zartman RE, Ling M (2015)

Porphyry deposits and oxidized magmas. Ore Geol Rev 65: 97–131.

Sun W, Liang H, Ling M, Zhan M, Ding X, Zhang H, Yang X, Li Y, Ireland TR, Wei Q, Fan W (2013) The link between reduced porphyry copper deposits and oxidized magmas. Geochim Cosmochim Acta 103: 263–275.

Sun SS, McDonough WF (1989) Chemical and isotopic systematics in ocean basalt: Implication for mantle composition and processes. In: Saunders, A.D, Norry, M.J. (Eds.), Magmatism in the Ocean Basins. 42. Geological Society of London Special Publications, pp 313–345.

Smith, M.P, Yardley, B.W.D, 1996. The boron isotopic composition of tourmaline as a guide to fluid processes in the southwestern England orefield: an ion microprobe study. Geochim Cosmochim Acta 60, 1415–1427.

Trumbull RB, Beurlen H, Wiedenbeck M, Soares DR (2013) The diversity of B-isotope variations in tourmaline from rare-element pegmatites in the Borborema Province of Brazil. Chem Geol 352: 47–62.

Trumbull RB, Chaussidon M (1999) Chemical and boron isotopic composition of magmatic and hydrothermal tourmalines from the Sinceni granite–pegmatite system in Swaziland. Chem Geol 153: 125–137.

Trumbull RB, Krienitz MS, Gottesmann B, Wiedenbeck M (2008) Chemical and boron isotope variations in tourmalines from an S-type granite and its source rocks: the Erongo granite and tourmalinites in the Damara Belt, Namibia. Contrib Mineral Petrol 155: 1–18.

Trumbull RB, Slack JF (2018) Boron isotopes in the continental crust: Granites, pegmatites, felsic volcanic rocks, and related ore deposits. In: Marschall, H, Foster, G. (Eds.), Boron Isotopes: The Fifth Element. Springer, Switzerland, pp. 249–272.

Trumbull RB, Slack JF, Krienitz M-S, Belkin HE, Wiedenbeck M (2011) Fluid sources and metallogenesis in the Blackbird Co–Cu–Au–Bi–Y–REE district, Idaho, USA: insights from major-element and boron isotopic compositions of tourmaline. Can Min 49:225–244

Tornos F, Wiedenbeck M, Velasco F (2012) The boron isotope geochemistry of tourmaline-rich alteration in the IOCG systems of northern Chile: implications for a magmatic-hydrothermal origin. Miner Deposita 47: 483–499.

Tonarini S, Dini A, Pezzotta F, Leeman WP (1998) Boron isotopic composition of zoned (schorl-elbaite) tourmalines, Mt. Capanne Li-Cs pegmatites, Elba (Italy). Eur J Mineral 10: 941–951.

Tonarini S, Pennisi M, Adorni-Bracces, A, Dini A, Ferrara G, Gonfiantini R, Wiedenbeck M, Gröning, M (2003) Intercomparison of boron isotope and concentration measurements. Part I: selection, preparation and homogeneity tests of the intercomparison materials. Geostand Geoanal Res 27: 21–39.

Van Hinsberg VJ (2011a) Preliminary experimental data on trace-element partitioning between tourmaline and silicate melt. Can Mineral 49: 153–163.

van Hinsberg VJ, Henry DJ, Dutrow BL (2011b) Tourmaline as a petrologic forensic mineral: a unique recorder of its geologic past. Elements 7: 327–332.

van Hinsberg VJ, Schumacher JC, Kearns S, Mason PRD, Franz G (2006) Hourglass sector zoning in metamorphic tourmaline and resultant major and trace-element fractionation. Am Mineral 91: 717–728.

Wang DH, Chen YC, Chen ZH, Liu SB, Xu JX, Zhang JJ, Zeng ZL, Chen FW, Li HQ, Guo CL (2007) Assessment on mineral resource in Nanling region and suggestion for further prospecting. Act Geol Sin 81: 882–890 (In Chinese with English abstract).

Wang DZ, Shu LS (2012) Late Mesozoic basin and range tectonics and related magmatism in Southeast China. Geosci Front 3: 109–124.

Wood SA (1990) The aqueous geochemistry of the rare-earth elements and yttrium: 2. theoretical predictions of speciation in hydrothermal solutions to 350 °C at saturation water vapor pres-sure. Chem Geol 88: 99–125.

Wu GY, Pan ZF, Hou ZQ, Li JD, Che LI, Chen Q (2005) Ore body distribution pattern, ore-controlling factors and prospecting potentiality in the Dayishan tin deposit, Hunan Province. Geol Prospect 41: 6–11 (in Chinese with English abstract).

Xavier RP, Wiedenbeck M, Trumbull RB, Dreher AM, Monteiro LVS, Rhed, D, Araújo CEG, Torresi I (2008) B-isotopes fingerprint marine evaporites as the source of high-salinity ore fluids in iron oxide copper-gold deposits, Carajás Mineral Province. Geology 36: 743–746.

Yao J, Shu L, Cawood PA, Li Y (2016) Delineating and characterizing the boundary of the Cathaysia block and the Jiangnan orogenic belt in South China. Precambrian Res 275: 265–277.

Yang LZ, Wu XB, Cao JY, Hu B, Zhang XW, Gong YS, Liu WD (2018) Geochronology, Petrology, and Genesis of Two Granitic Plutons of the Xianghualing Ore Field in South Hunan Province: Constraints from Zircon U–Pb Dating, Geochemistry, and Lu–Hf Isotopic Compositions. Minerals 8: 213–224.

Yang SY, Jiang SY, Palmer MR (2015a) Chemical and boron isotopic compositions of tourmaline from the Nyalam leucogranites, South Tibetan Himalaya: Implication for their formation from B-rich melt to hydrothermal fluids. Chem Geol 419: 102–113.

Yang SY, Jiang SY, Zhao KD, Dai BZ, Yang T (2015b) Tourmaline as a recorder of magmatic-hydro-thermal evolution: an in situ major and trace element analysis of tourmaline from the Qitianling batholith, South China. Contrib Mineral Petrol 170: 1–21.

Yavuz F, Karacaya N, Yildirim DK, Karakaya MÇ, Kumral M (2013) A Windows program for calculation and classification of tourmaline-super group (IMA-2011). Comput Geosci 63: 70–87.

Yu JH, Wang LJ, O'Reilly SY, Griffin WL, Zhang M, Li, CZ, Shu LS (2009) A Paleoproterozoic orogeny recorded in a long-lived cratonic remnant (Wuyishan terrane), eastern Cathaysia Block, China. Precambrian Res 174: 347–363.

Yuan SD, Mao JW, Zhao PL, Yun YB (2018) Geochronology and petrogenesis of the Qibaoshan Cu-polymetallicdeposit, northeastern Hunan Province: Implications for the metal source and metallogenic evolution of the intracontinental Qinhang Cu-polymetallic belt, South China. Lithos 302: 519–534.

Zeng QW, Peng LJ, Tian WW, Qian T, You GH, Chen YL, Long L (2016) Deep ore exploration of the Baishaziling tungsten-tin ore district, Dayishan pluton, Hunan. Geol China: 1625–1636 (in Chinese with English abstract).

Zhang C, Sun W, Wang J, Zhang L, Sun S, Wu K (2017) Oxygen fugacity and porphyry mineralization: A zircon perspective of Dexing porphyry Cu deposit, China. Geochim Cosmochim Acta 206: 343-363.

Zhang W, Chen H, Peng L, Zhao L, Huang J, Lu W, Liang P, Lai C (2018) Discriminating hydrothermal fluid sources using tourmaline boron isotopes: Example from Bailingshan Fe deposit in the Eastern Tianshan, NW China. Ore Geol Rev 98: 28-37.

Zhang XJ, Luo H, Wu ZH, Fan XW, Xiong J, Yang J, Mao JY (2014) Rb–Sr Isochron Age and Its Geological Significance of Baishaziling Tin deposit in Dayishan Ore Field, Hunan Province. Earth Sci 39: 1322–1332 (in Chinese with English abstract).

Zhao JH, Zhou MF, Yan DP, Zheng JP, Li JW (2011) Reappraisal of the ages of Neoproterozoic strata in South China: no connection with the Grenvillian orogeny. Geology 39: 299–302.

Zhao HD, Zhao KD, Palmer MR, Jiang SY (2019) In-situ elemental and boron isotopic variations of tourmaline from the Sanfang granite, South China: Insights into magmatic-hydrothermal evolution. Chem Geol 504: 190–204.

Zhao ZX, Xu ZW, Zuo CH, Lu JJ, Wang RC, Miao BH, Lu R (2017) Emplacement time and material source of Southern Dayishan granitic batholith (Taipingshan body), Guiyang City, Huan Province. Geol Review 63: 395–408 (in Chinese with English abstract).

Zheng Z, Chen YJ, Deng XH, Yue SW, Chen HJ, Wang QF (2019) Tourmaline geochemistry and boron isotopic variations as a guide to fluid evolution in the Qiman Tagh W–Sn belt, East Kunlun, China. Geosci Front 10: 569–580.

Zheng Z, Deng XH, Chen HJ, Yue SW, Dong LH, Q, X, Chen YJ (2016) Fluid sources and metallogenesis in the Baiganhu W–Sn deposit, East Kunlun, NW China: Insights from chemical and boron isotopic compositions of tourmaline. Ore Geol Rev 72: 1129–1142.

Zhou HX, Yang GH, Jiang ZH, Chen QC (2005) Geologocal characteristics and origin of the Dayishan tin orefield in Nanling region. Geology and Mineral Resources of South China 27: 87–94 (in Chinese with English abstract).

Zhou MF, Gao JF, Zhao Z, Zhao WW (2018) Introduction to the special issue of Mesozoic W-Sn deposits in South China. Ore Geol Rev 101: 432–436.

Zhou Q, Li W, Wang G, Liu Z, Lai Y, Huang J, Yan G, Zhang Q (2019) Chemical and boron isotopic composition of tourmaline from the Conadong leucogranite-pegmatite system in South Tibet. Lithos 326-327: 529-539.

Zhou XM, Sun T, Shen WZ, Shu LS, Niu YL (2006) Petrogenesis of Mesozoic granitoids and volcanic rocks in South China: A response to tectonic evolution. Episodes 29: 26–33.

Figure captions

Fig. 1 (a) Tectonic map of China; (b) Simplified geologic map, showing the distribution of granites in South China; (c) The range of Nangling (modified after Sun et al., 2006; Che et al., 2019).

Fig. 2 Regional geological map of Dayishan in Hunan Province, South China (modified after Zhao et al., 2017; Sun et al., 2018).

Fig. 3 Photographs and microstructures of tourmaline samples in the granite from Dayishan. (a) Photograph of hand specimens of monzogranite, showing coarse-grained and medium–fine-grained, whose boundary is represented by a red line; (b) Photograph of hand specimens of Tur-G1; (c) Photograph of hand specimens of Tur-G2; (d, e) Photographs of Tur-G1 enriched regions, showing sub-euhedral to anhedral morphology, yellowish-brown color; (f, g, h) Photographs of Tur-G2 enriched regions, which exhibit yellowish-brown in color, and are typically replaced by K-feldspar. (i) BSE images of Tur-G1, showing no oscillatory zoning and narrow $\delta^{11}B$ variation between core and rim. (j, k) BSE images of Tur-G2, showing no oscillatory zoning. In (i, j, k), the filled red circles represent analyzed spots for boron isotope. Tur = tourmaline, Qtz = quartz, Pl= plagioclase, Klf = k-feldspar, Mc = Mica, Fl = fluorite.

Fig. 4 Photographs and microstructures of Tur-Gr from Dayishan. (a, b) Photographs of hand specimens of Tur-Gr, showing radial to dendritic morphologies with needlelike, long columnar or massive tourmaline aggregates; (c, d) Photographs of sub- to euhedral tourmalines which are optically zoned from yellowish-brown core (Tur-Gry) to blue rim (Tur-Grb); (e, f) BSE images of Tur-Gr tourmaline. Red circles and labels are analyzed spots for boron isotope. Tur = tourmaline, Qtz = quartz, Mc = Mica, Fl = fluorite, Py = pyrite.

Fig. 5 Photographs and microstructures of Tur-V from Dayishan. (a, b) Outcrop Photographs of Tur-V, showing radial to dendritic morphologies with needlelike, long columnar or massive tourmaline aggregates; (c, d) Photographs of tourmaline, exhibiting blue in color without optical zoning; (e, f) BSE images of tourmaline. Red circles and labels are analyzed spots for boron isotope. Tur = tourmaline, Qtz = quartz, Fl = fluorite.

Fig. 6 (a) Classification diagrams of all types of tourmalines from Dayishan based on X-site occupancy (modified after Henry et al., 2011); (b) Ternary Al-Fe-Mg diagrams showing compositional variations of tourmalines from the Shangbao deposit; (c) Ca-Fe-Mg ternary diagrams showing compositional variations of tourmalines from Dayishan. The fields classify the compositions of tourmalines from different rocks (Henry and Guidotti, 1985). Labelled fields are: 1 = Li-rich granitoids and associated pegmatites and aplites; 2 = Li-poor granitoids and associated pegmatites and aplites; 3 = Fe^{3+}-rich quartz–tourmaline rocks (hydrothermally altered granites); 4 = Metapelites and metapsammites coexisting with an Al-saturating phase; 5 = Metapelites and metapsammites not coexisting with an Al-saturating phase; 6 = Fe^{3+}-rich quartz–tourmaline rocks, calc silicate rocks, and metapelites; 7 = Low Ca metaultramafics and Cr, V-rich metasediments; 8 = Metacarbonates and metapyroxenites; 9 = Ca-rich metapelites, metapsammites, and calc-silicate rocks; 10 = Ca-poor metapelites, metapsammites, and quartz–tourmaline rocks; 11 = Metacarbonates; 12 = Metaultramafics. SHT = Sanfang hydrothermal tourmaline (Zhao et al., 2019); SMT = Sanfang magmatic tourmaline (Zhao et al., 2019); QHT = Qitianling hydrothermal tourmaline (Yang et al., 2015b).

Fig. 7 (a, b) Classification of tourmalines from Dayishan (modified after Trumbull and Chaussidon, 1999; Henry and Dutrow, 2012); (c – f) Chemical discrimination diagrams for tourmalines from Dayishan, showing their compositional evolution trends and exchange vectors (modified after Henry and Dutrow, 1990, 2012)

Fig. 8 Distributions of REE and trace elements of tourmalines from Dayishan. (a, c, e). Chondrite-normalized REE distribution patterns; (b, d, f) Spider diagrams of trace elements. The Chondrite-normalized and primitive mantle-normalized values are from Sun and McDonough, (1989).

Fig. 9 (a – i) Trace element variation diagrams of tourmalines from the Dayishan magmatic–hydrothermal system, showing the compositional differences between different types of tourmaline; (j – o) Selected element contents vs. Fe/(Fe + Mg) ratios in different types of tourmalines from the Dayishan granite.

Fig. 10 (a) Diagram showing limited variations of boron isotopic compositions in studied tourmalines; (b) Comparison of $\delta^{11}B$ values of tourmalines from various deposits and earth boron reservoirs. The $\delta^{11}B$ data of boron reservoirs are cited from Barth, (1993) and Marschall and Jiang, (2011). The referenced specific deposit $\delta^{11}B$ data of different types of granite are cited from Tornos et al. (2012), Iveson et al. (2016), Barton, (2014), Zhao et al. (2019), Zheng et al. (2019), Zheng et al. (2016), Smith and Yardley, (1996), Jiang, (2001), Duan et al. (2019).

Fig. 11 Boron isotope fractionation curves (after Marschall et al., 2009 and Büttner et al., 2016, using fractionation values from Meyer et al., 2008), assuming constant fluid temperatures between 700 and 350 °C. The initial $\delta^{11}B$ value is -14.84‰. See also supplementary Table D.

This is the peer-reviewed, final accepted version for American Mineralogist, published by the Mineralogical Society of America.
The published version is subject to change. Cite as Authors (Year) Title. American Mineralogist, in press.
DOI: https://doi.org/10.2138/am-2021-7591. http://www.minsocam.org/

Table 1 Characteristics of different tourmalines from the Dayishan.

Tourmaline type	Host lithology	Tourmaline content (vol. %)	Field Occurrence	coexist mineral	Microscopic features
Tur-G1	Coarse-grained monzogranite	2-3	Black, short columnar-like crystal, < 2mm in length	Quartz, plagioclase, K feldspar apatite, zircon, fluorite, Mica,	Sub-euhedral to anhedral grains, exhibit yellowish-brown in color and without optical zoning.
Tur-G2	Medium-fine grained monzogranite	5-7	Black, needle- or short columnar-like crystals, 1-5 mm in length	Quartz, plagioclase apatite, zircon, fluorite, Mica, K feldspar	Sub-euhedral to anhedral grains, exhibit yellowish -brown in color without optical zoning similar to that of Tur-G1.
Tur-Gr (Tur-Grb, Tur-Gry)	Greisen	20-30	Black, Reticulate vein- or cluster- like aggregate,	Quartz, Mica, fluorite, pyrite, chalcopyrite,	Euhedral to Sub-euhedral grains. yellow-brown cores (Tur-Gry) and blue rims (Tur-Grb),
Tur-V	Quartz vein	10-20	Black, radial like- crystal, up to 7cm in length	Quartz, fluorite	Euhedral to sub-euhedral grains. exhibit blue in color without optical zoning

Table 2 Major element compositions of tourmalines from the Dayishan.

Type	Tur-G1 (n=20)		Tur-G2 (n=26)		Tur-Gry (n=26)		Tur-Grb (n=23)		Tur-Vb (n=38)	
(wt. %)	Range	Mean	Range	Mean	Range	Mean	Range	Mean	Range	Mean
SiO_2	31.87-35.29	0.17	32-12-34.71	33.16	33.90-35.63	34.60	34.10-35.81	34.72	33.81-35.42	34.82
TiO_2	0.17-0.55	0.37	0.12-0.76	0.44	0.03-0.94	0.38	0.01-0.53	0.12	0.00-0.27	0.07
Al_2O_3	31.86-33.82	32.86	31.61-33.81	32.59	30.31-34.05	32.83	31.06-33.70	32.30	30.29-33.94	32.52
FeO	12.29-14.91	13.53	12.53-14.46	13.53	12.38-16.08	13.84	12.52-17.36	15.44	13.67-16.79	15.20
MnO	014-0.52	0.29	0.14-0.53	0.26	0.06-0.51	0.27	0.10-0.47	0.28	0.25-0.56	0.35
MgO	2.23-4.28	3.33	1.27-4.22	3.05	0.91-3.52	1.69	0.03-1.72	0.43	0.01-0.23	0.07
CaO	0.04-0.41	0.16	0.05-0.22	0.15	0.09-0.26	0.16	0.02-0.30	0.12	0.00-0.12	0.06
Na_2O	1.47-2.26	1.99	1.57-2.18	1.95	1.84-2.16	1.93	1..45-2.22	1.95	1.24-2.25	1.85
K_2O	0.02-0.07	0.04	0.02-0.08	0.04	0.03-0.08	0.05	0.02-0.07	0.04	0.01-0.07	0.04
F	0.00-0.19	0.04	0.00-0.27	0.06	0.00-0.19	0.06	0.00-0.21	0.03	0.00-0.14	0.02
B_2O_3*	10.08-10.69	10.27	9.92-10.41	10.19	9.94-10.43	10.19	9.92-10.24	10.04	9.81-10.17	10.00
H_2O*	3.19-3.39	3.27	3.12-3.29	3.22	3.13-3.28	3.20	3.06-3.26	3.18	2.98-3.26	3.14
Total	98.08-102.66	99.27	97.20-99.60	98.60	98.15-100.42	99.17	97.99-99.40	98.56	96.95-99.04	98.04
apfu.										
B	3.00-3.04	3.02	3.00-3.05	3.02	2.97-3.01	3.00	2.97-3.00	2.99	2.97-3.00	2.98
T-site										
Si	5.46-5.79	5.60	5.45-5.86	5.66	5.75-6.03	5.91	5.94-6.13	6.01	5.95-6.16	6.05
Al	0.21-0.51	0.37	0.14-0.51	0.33	0.00-0.25	0.10	0.00-0.07	0.02	0.00-0.05	0.00
Z-site										
Al	5.98-6.00	6.00	6.00-6.00	6.00	6.00-6.00	6.00	6.00-6.00	6.00	6.00-6.00	6.00
Mg	0.00-0.02	0.00	0.00-0.00	0.00	0.00-0.02	0.00	0.00-0.02	0.00	0.00-0.00	0.00
Fe	0.00-0.00	0.00	0.00-0.00	0.00	0.00-0.00	0.00	0.00-0.00	0.00	0.00-0.00	0.00
Y-site										

DOI: https://doi.org/10.2138/am-2021-7591. http://www.minsocam.org/

Al	0.00-0.44	0.18	0.00-0.58	0.22	0.24-0.70	0.51	0.34-0.87	0.57	0.33-0.87	0.66
Ti	0.02-0.07	0.05	0.03-0.10	0.06	0.00-0.12	0.05	0.00-0.07	0.02	0.00-0.04	0.01
Fe	1.70-2.11	1.92	1.76-2.09	1.93	1.75-2.35	1.98	1.78-2.54	2.24	1.97-2.49	2.21
Mg	0.57-1.08	0.84	0.33-1.07	0.77	0.24-0.88	0.43	0.01-0.44	0.11	0.00-0.06	0.02
Mn	1.70-2.11	1.92	0.02-0.08	0.04	0.01-0.08	0.04	0.02-0.07	0.04	0.04-0.08	0.05
∑Y	3.00-3.04	3.02	3.00-3.05	3.02	2.97-3.01	3.00	2.87-3.00	2.97	2.84-3.00	2.95
X-site										
Ca	0.01-0.08	0.03	0.01-0.04	0.03	0.01-0.05	0.03	0.00-0.06	0.02	0.00-0.02	0.01
Na	0.47-0.76	0.65	0.51-0.73	0.65	0.48-0.73	0.64	0.48-0.75	0.65	0.42-0.77	0.62
K	0.01-0.02	0.01	0.00-0.02	0.01	0.01-0.02	0.01	0.00-0.02	0.01	0.00-0.02	0.01
Xvac	0.21-0.51	0.31	0.22-0.46	0.32	0.23-0.48	0.32	0.22-0.51	0.32	0.21-0.57	0.36

The structural formulae are calculated on the basis of 15 cations in the tetrahedral and octahedral sites (T + Z + Y) of the tourmaline.

Table 3 LA-ICP-MS trace element compositions of tourmalines from the Dayishan.

Type	Tur-G1 (n=8)		Tur-G2 (n=9)		Tur-Gry (n=13)		Tur-Grb (n=12)		Tur-Vb (n=13)	
(ppm)	Range	Mean	Range	Mean	Range	Mean	Range	Mean	Range	Mean
Li	232-331	274	264-303	278	165-328	226	156-369	255	159-487	278
Sc	36.73-51.49	44.81	19.19-35.50	29.73	1.28-65.98	26.92	0.00-8.53	1.85	0.00-4.26	1.88
V	22.80-50.34	38.03	18.44-68.97	40.68	0.00-64.10	33.94	0.00-8.90	2.72	0.00-7.76	2.01
Co	12.60-15.97	14.19	11.01-17.06	14.07	9.92-17.77	14.10	9.75-17.50	13.01	11.11-13.35	12.08
Zn	376-422	394	377-401	387	351-669	430	444-742	630	525-673	585
Pb	1.47-2.62	1.95	1.07-3.47	2.06	1.10-4.21	2.35	1.54-4.91	3.38	1.02-5.70	3.08
Cu	0.00-1.12	0.35	0.00-1.00	0.30	0.00-2.50	0.70	0.00-5.72	2.60	0.47-4.79	1.73
Rb	0.00-0..21	0.07	0.00-0.45	0.23	0.02-2.48	0.32	0.00-0.26	0.13	0.05-0.47	0.20
Sr	0.27-0.39	0.34	0.76-2.83	1.87	0.29-26.30	4.66	2.43-28.32	14.05	0.85-4.22	2.29
Y	0.05-0.95	0.20	0.03-0.19	0.0	0.01-0.12	0.08	0.00-0.11	0.03	0.01-0.25	0.09
Zr	0.00-1.51	1.10	0.00-2.90	0.99	1.31-4.74	2.48	0.07-3.21	1.51	0.01-2.86	1.16
Nb	0.81-1.74	1.24	1.87-3.20	2.53	0.11-3.15	1.15	0.03-1.38	0.55	0.86-2.80	1.72
Sn	113-154	137	127-160	144	115-166	134	121-418	229	202-485	336
Ba	0.00-0.27	0.13	0.00-0.40	0.18	0.01-0.08	0.04	0.06-0.23	0.16	0.01-0.86	0.20
La	2.62-6.75	4.86	1.41-2.65	2.27	0.24-4.80	2.33	0.51-2.74	1.78	0.16-2.06	0.90
Ce	7.06-16.83	13.14	2.90-4.16	3.68	0.53-14.00	4.64	0.66-3.43	2.24	0.25-2.13	1.02
Pr	0.80-1.80	1.34	0.23-0.38	0.29	0.03-1.50	0.43	0.01-0.26	0.15	0.01-0.12	0.06
Nd	2.68-4.88	4.12	0.66-1.39	0.98	0.08-4.44	1.36	0.03-0.60	0.35	0.04-0.31	0.14
Sm	0.45-1.83	1.14	0.12-0.36	0.19	0.02-1.03	0.25	0.01-0.08	0.04	0.01-0.11	0.03
Eu	0.01-0.02	0.01	0.02-0.04	0.03	0.00-0.04	0.02	0.03-0.13	0.06	0.00-0.04	0.02
Gd	0.16-0.40	0.27	0.09-0.31	0.15	0.02-0.33	0.12	0.02-0.16	0.09	0.00-0.08	0.02
Tb	0.01-0.03	0.02	0.01-0.02	0.01	0.00-0.03	0.01	0.00-0.01	0.00	0.00-0.02	0.01
Dy	0.00-0.17	0.08	0.00-0.06	0.04	0.01-0.06	0.03	0.01-0.05	0.03	0.01-0.07	0.03

Ho	0.00-0.02	0.01	0.00-0.01	0.01	0.00-0.01	0.01	0.00-0.01	0.01	0.00-0.02	0.01
Er	0.00-0.01	0.01	0.00-0.02	0.01	0.01-0.07	0.03	0.01-0.07	0.03	0.00-0.08	0.03
Tm	0.00-0.02	0.01	0.00-0.01	0.01	0.00-0.03	0.01	0.00-0.03	0.01	0.00-0.02	0.01
Yb	0.00-0.09	0.04	0.00-0.008	0.04	0.01-0.30	0.07	0.02-0.49	0.12	0.02-0.30	0.13
Lu	0.00-0.01	0.00	0.00-0.01	0.00	0.00-0.06	0.02	0.00-0.16	0.03	0.00-0.12	0.05
Hf	0.01-0.04	0.02	0.03-0.08	0.06	0.00-0.50	0.13	0.00-0.19	0.04	0.03-0.58	0.23
Ta	0.27-0.98	0.67	1.39-3.63	2.27	0.12-28.58	3.53	0.07-7.39	1.83	3.42-15.65	8.00
W	0.00-0.05	0.01	0.00-0.13	0.02	0.00-0.16	0.06	0.00-0.14	0.04	0.00-0.15	0.06
Th	0.01-0.06	0.03	0.02-0.15	0.06	0.00-0.17	0.05	0.00-0.48	0.06	0.01-0.12	0.04
U	0.00-0.01	0.00	0.00-0.01	0.00	0.00-0.05	0.02	0.00-0.40	0.07	0.00-0.05	0.02
REE	14.63-31.30	25.05	6.17-8.68	7.70	1.10-26.35	9.33	2.09-7.06	4.95	0.94-4.67	2.45

Table 4 Boron isotope values for tourmaline from the Dayishan.

Analysis no.	Type	$\delta^{11}B$ (‰)	1SD (‰)
DYS-H1-1	Tur-G1	-14.8	0.3
DYS-H1-2	Tur-G1	-14.82	0.3
DYS-H1-4	Tur-G1	-15.24	0.4
DYS-H1-6	Tur-G1	-15.16	0.2
DYS-H2-1	Tur-G1	-14.17	0.2
DYS-H2-2	Tur-G1	-15.01	0.2
DYS-H2-4	Tur-G1	-14.61	0.3
DYS-H2-5	Tur-G1	-14.47	0.2
DYS-H2-6	Tur-G1	-14.94	0.3
DYS-H3-1	Tur-G1 (core)	-14.15	0.4
DYS-H3-1	Tur-G1 (rim)	-14.29	0.3
DYS-H3-3	Tur-G1	-15.55	0.3
DYS-H3-8	Tur-G1	-14.35	0.3
DYS-H1-7	Tur-G1 (core)	-14.57	0.3
DYS-H1-7	Tur-G1 (rim)	-14.63	0.2
DYS-H3-9	Tur-G1 (core)	-14.92	0.3
DYS-H3-9	Tur-G1 (rim)	-14.86	0.3
DYS-H4-1	Tur-G2	-15.51	0.2
DYS-H4-2	Tur-G2	-15.31	0.4
DYS-H4-3	Tur-G2	-15.42	0.2
DYS-H4-7	Tur-G2	-14.95	0.3
DYS-H5-1	Tur-G2 (core)	-14.68	0.4
DYS-H5-1	Tur-G2 (rim)	-15.35	0.2
DYS-H5-3	Tur-G2	-14.84	0.4
DYS-H5-5	Tur-G2	-15.27	0.2
DYS-H5-6	Tur-G2	-15.19	0.3
DYS-H5-8	Tur-G2	-14.09	0.3
DYS-H6-2	Tur-G2	-14.72	0.2
DYS-H6-3	Tur-G2	-14.81	0.3
DYS-H6-4	Tur-G2	-14.64	0.4
DYS-H4-9	Tur-G2 (core)	-14.85	0.4
DYS-H4-9	Tur-G2 (rim)	-14.73	0.4
DYS-H6-9	Tur-G2 (core)	-14.92	0.3
DYS-H6-9	Tur-G2 (rim)	-14.87	0.3
DYS-G7-5	Tur-Gry	-15.02	0.4
DYS-G7-13	Tur-Gry	-14.84	0.4
DYS-G8-1	Tur-Gry (core)	-14.43	0.2
DYS-G8-1	Tur-Gry (rim)	-14.60	0.2
DYS-G8-9	Tur-Gry	-15.46	0.4
DYS-G8-13	Tur-Gry	-15.09	0.4
DYS-G8-15	Tur-Gry	-15.13	0.3
DYS-G9-3	Tur-Gry	-15.33	0.3

DOI: https://doi.org/10.2138/am-2021-7591. http://www.minsocam.org/

DYS-G9-9	Tur-Gry	-15.58	0.2
DYS-G9-13	Tur-Gry	-14.77	0.2
DYS-G9-15	Tur-Gry	-14.69	0.4
DYS-G9-17	Tur-Gry	-14.61	0.3
DYS-G9-19	Tur-Gry	-15.03	0.2
DYS-G7-6	Tur-Grb	-14.91	0.2
DYS-G7-14	Tur-Grb	-15.83	0.2
DYS-G8-2	Tur-Grb	-16.15	0.2
DYS-G8-6	Tur-Grb	-15.66	0.2
DYS-G8-10	Tur-Grb	-15.41	0.4
DYS-G8-14	Tur-Grb	-15.75	0.2
DYS-G9-16	Tur-Grb	-15.64	0.3
DYS-G9-4	Tur-Grb	-15.76	0.4
DYS-G9-10	Tur-Grb	-15.43	0.2
DYS-G9-14	Tur-Grb	-16.02	0.3
DYS-G9-16	Tur-Grb	-15.43	0.4
DYS-G9-18	Tur-Grb	-15.29	0.4
DYS-G9-20	Tur-Grb	-16.11	0.4
DYS-V10-1	Tur-V	-15.42	0.2
DYS-V10-2	Tur-V	-15.84	0.3
DYS-V10-4	Tur-V	-15.71	0.4
DYS-V10-7	Tur-V	-15.88	0.4
DYS-V11-2	Tur-V	-16.18	0.2
DYS-V11-3	Tur-V	-15.34	0.3
DYS-V11-5	Tur-V	-16.22	0.4
DYS-V11-6	Tur-V	-15.48	0.2
DYS-V12-3	Tur-V	-15.39	0.4
DYS-V12-5	Tur-V	-16.07	0.2
DYS-V13-3	Tur-V	-15.9	0.3
DYS-V13-4	Tur-V	-16.31	0.4
DYS-V13-9	Tur-V	-15.79	0.4

Figure 1

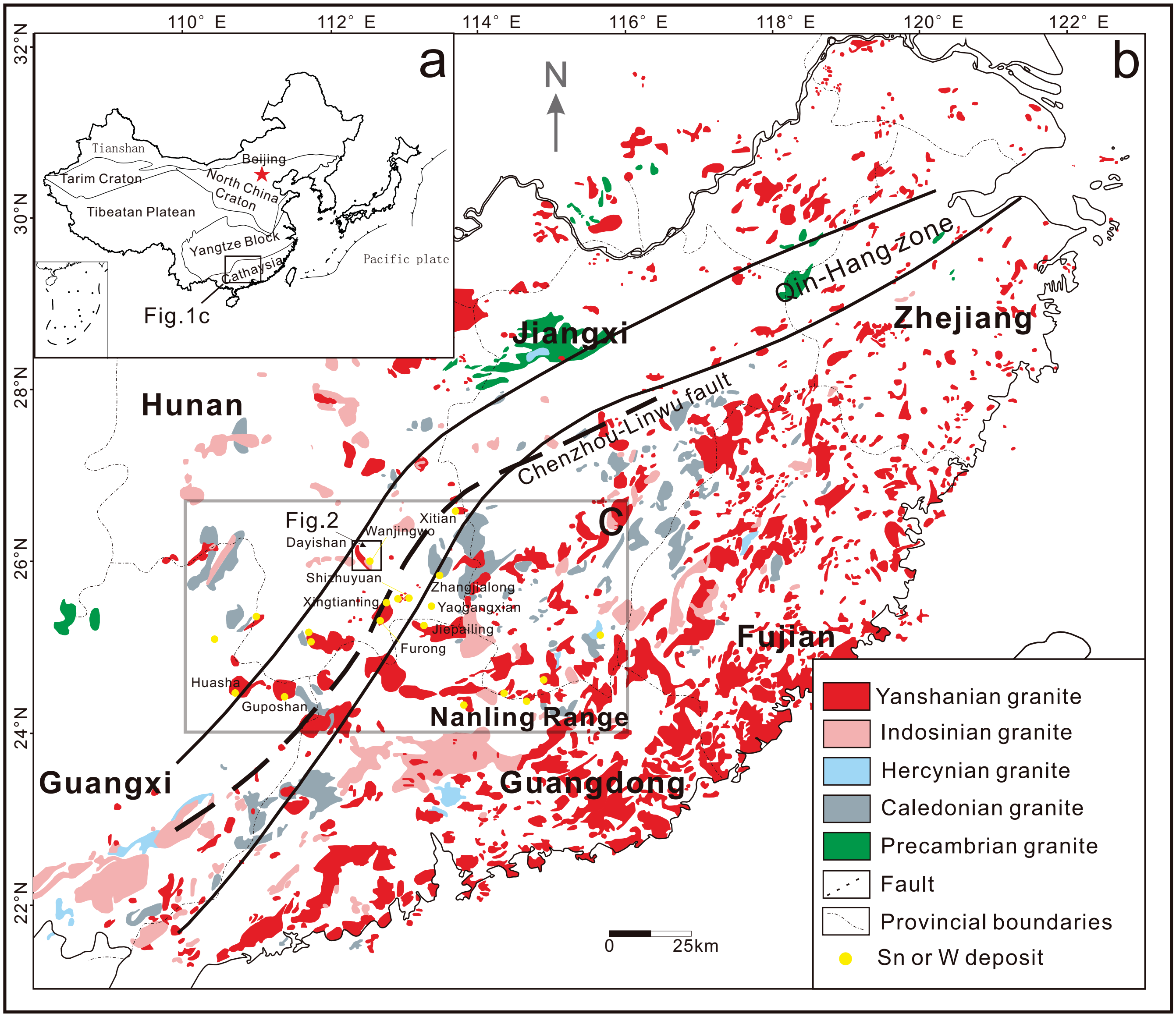
a
b
N
Tianshan
Tarim Craton
Beijing
North China Craton
Tibeatan Platean
Yangtze Block
Cathaysia
Pacific plate
Fig.1c
Hunan
Jiangxi
Zhejiang
Fujian
Guangxi
Guangdong
Qin-Hang zone
Chenzhou-Linwu fault
Nanling Range
Fig.2
c
Dayishan
Wanjingwo
Xitian
Shizhuyuan
Xingtianling
Zhangjialong
Yaogangxian
Jiepailing
Furong
Huasha
Guposhan
110° E
112° E
114° E
116° E
118° E
120° E
122° E
32°N
30°N
28°N
26°N
24°N
22°N
0
25km
Yanshanian granite
Indosinian granite
Hercynian granite
Caledonian granite
Precambrian granite
Fault
Provincial boundaries
Sn or W deposit

This is the peer-reviewed, final accepted version for American Mineralogist, published by the Mineralogical Society of America.
The published version is subject to change. Cite as Authors (Year) Title. American Mineralogist, in press.
DOI: https://doi.org/10.2138/am-2021-7591. http://www.minsocam.org/

Figure 2

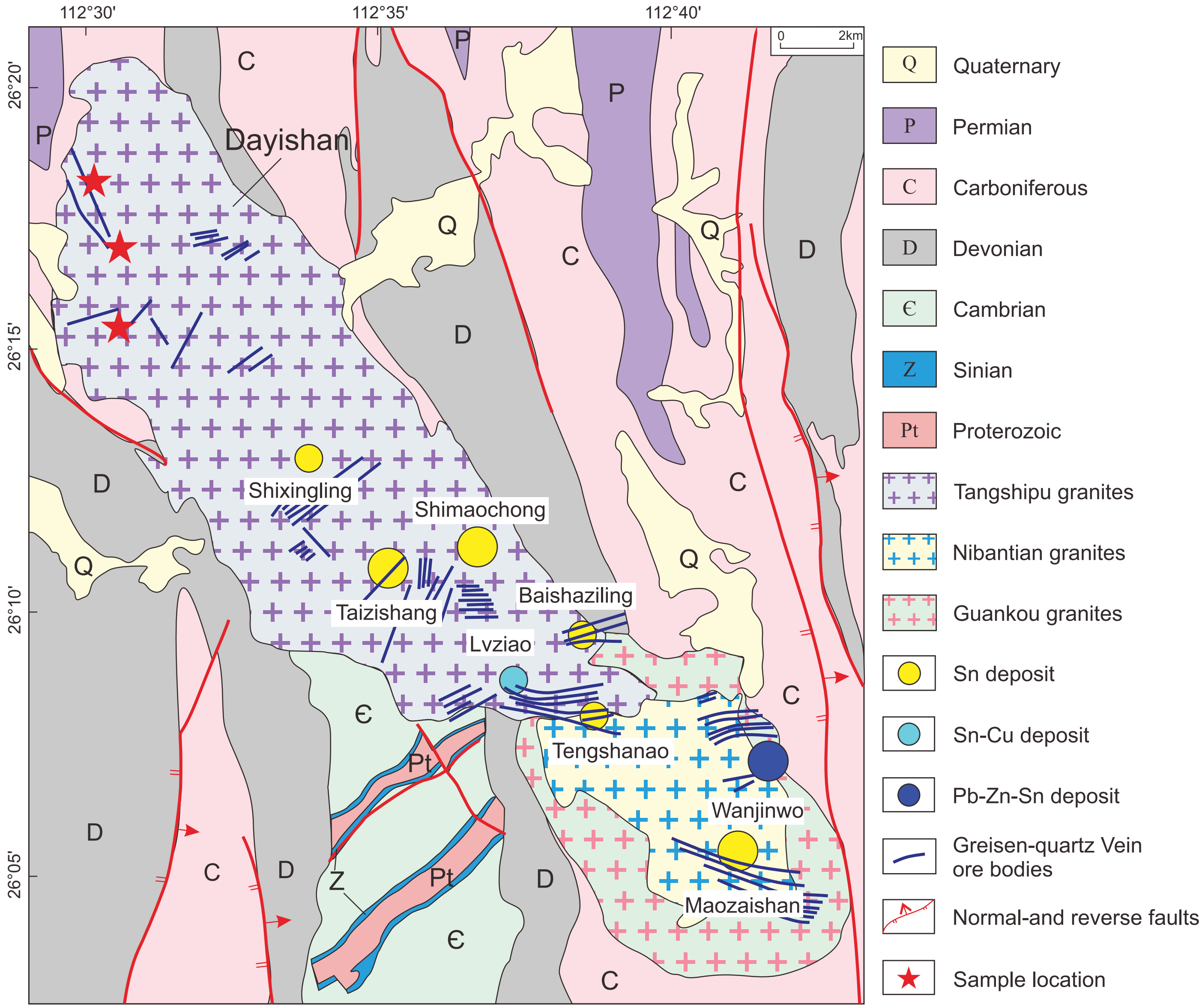

Figure 3

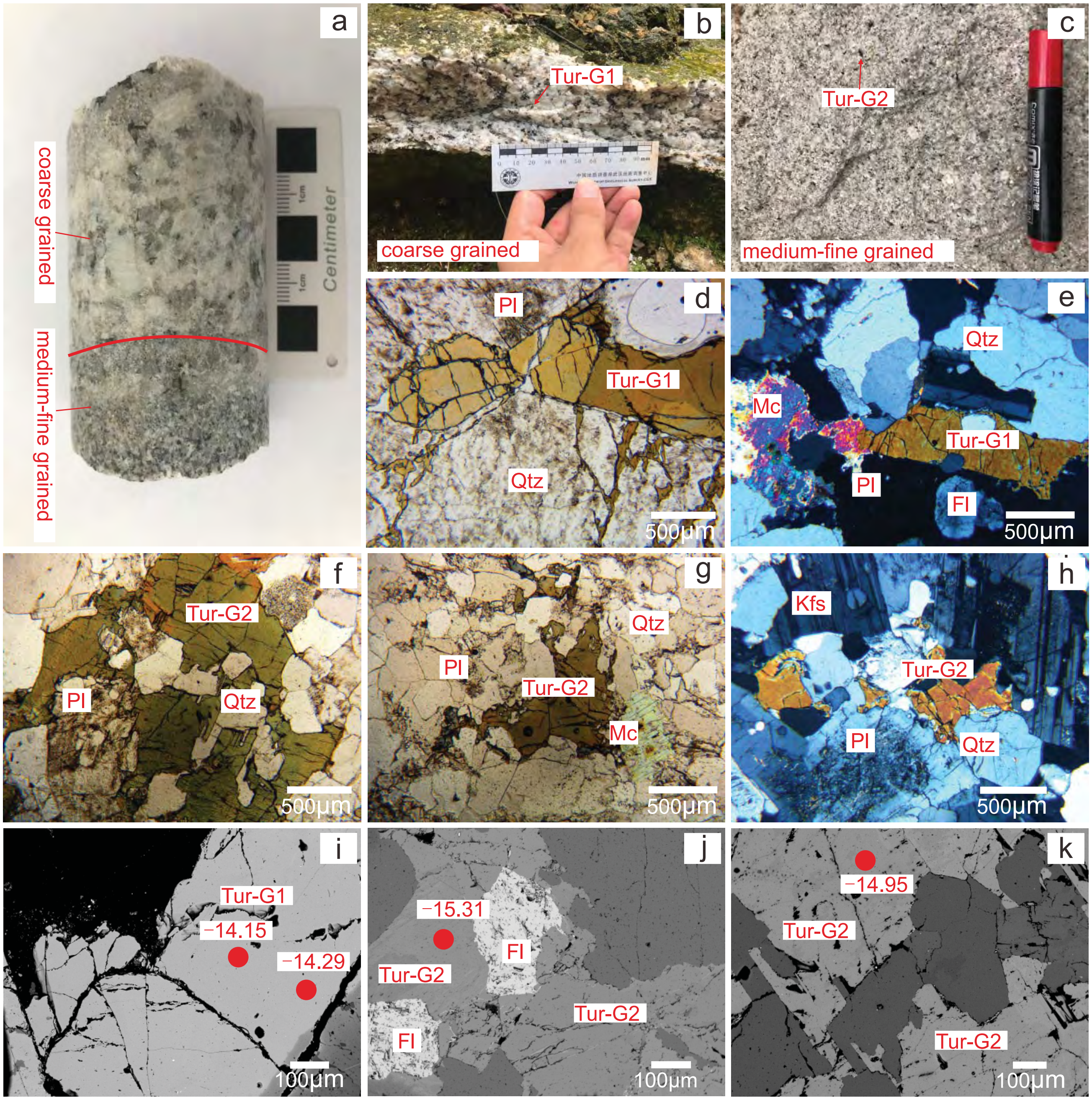
a
coarse grained
medium-fine grained
Centimeter
1cm
1cm
b
Tur-G1
coarse grained
c
Tur-G2
medium-fine grained
d
Pl
Tur-G1
Qtz
500μm
e
Qtz
Mc
Tur-G1
Pl
Fl
500μm
f
Tur-G2
Pl
Qtz
500μm
g
Qtz
Pl
Tur-G2
Mc
500μm
h
Kfs
Tur-G2
Pl
Qtz
500μm
i
Tur-G1
−14.15
−14.29
100μm
j
−15.31
Fl
Tur-G2
Tur-G2
Fl
100μm
k
−14.95
Tur-G2
Tur-G2
100μm

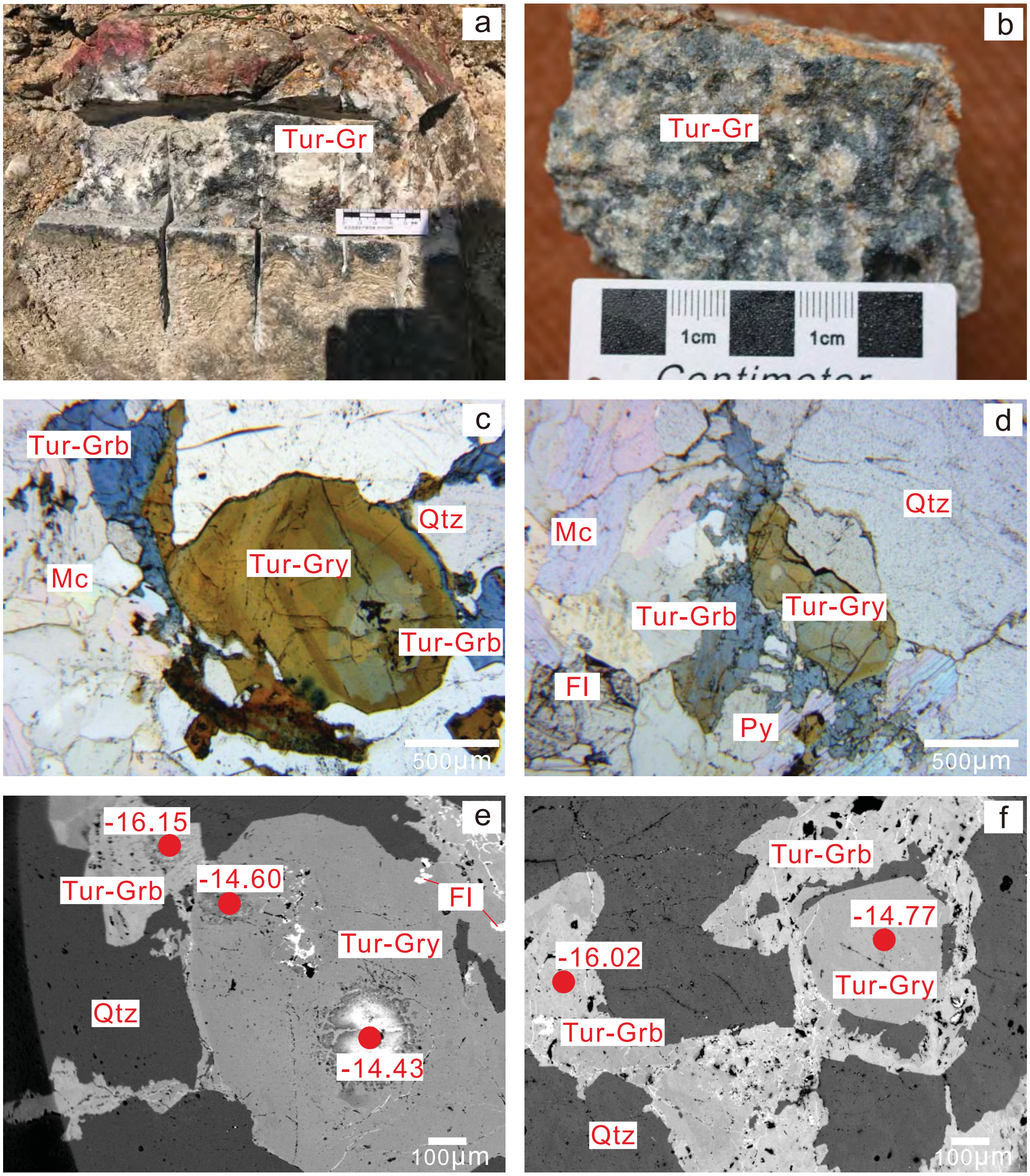
a
Tur-Gr
b
Tur-Gr
1cm
1cm
c
Tur-Grb
Qtz
Tur-Gry
Mc
Tur-Grb
500μm
d
Qtz
Mc
Tur-Grb
Tur-Gry
Fl
Py
500μm
e
-16.15
Tur-Grb
-14.60
Fl
Tur-Gry
Qtz
-14.43
100μm
f
Tur-Grb
-14.77
-16.02
Tur-Gry
Tur-Grb
Qtz
100μm

This is the peer-reviewed, final accepted version for American Mineralogist, published by the Mineralogical Society of America.
The published version is subject to change. Cite as Authors (Year) Title. American Mineralogist, in press.
DOI: https://doi.org/10.2138/am-2021-7591. http://www.minsocam.org/

Figure 5

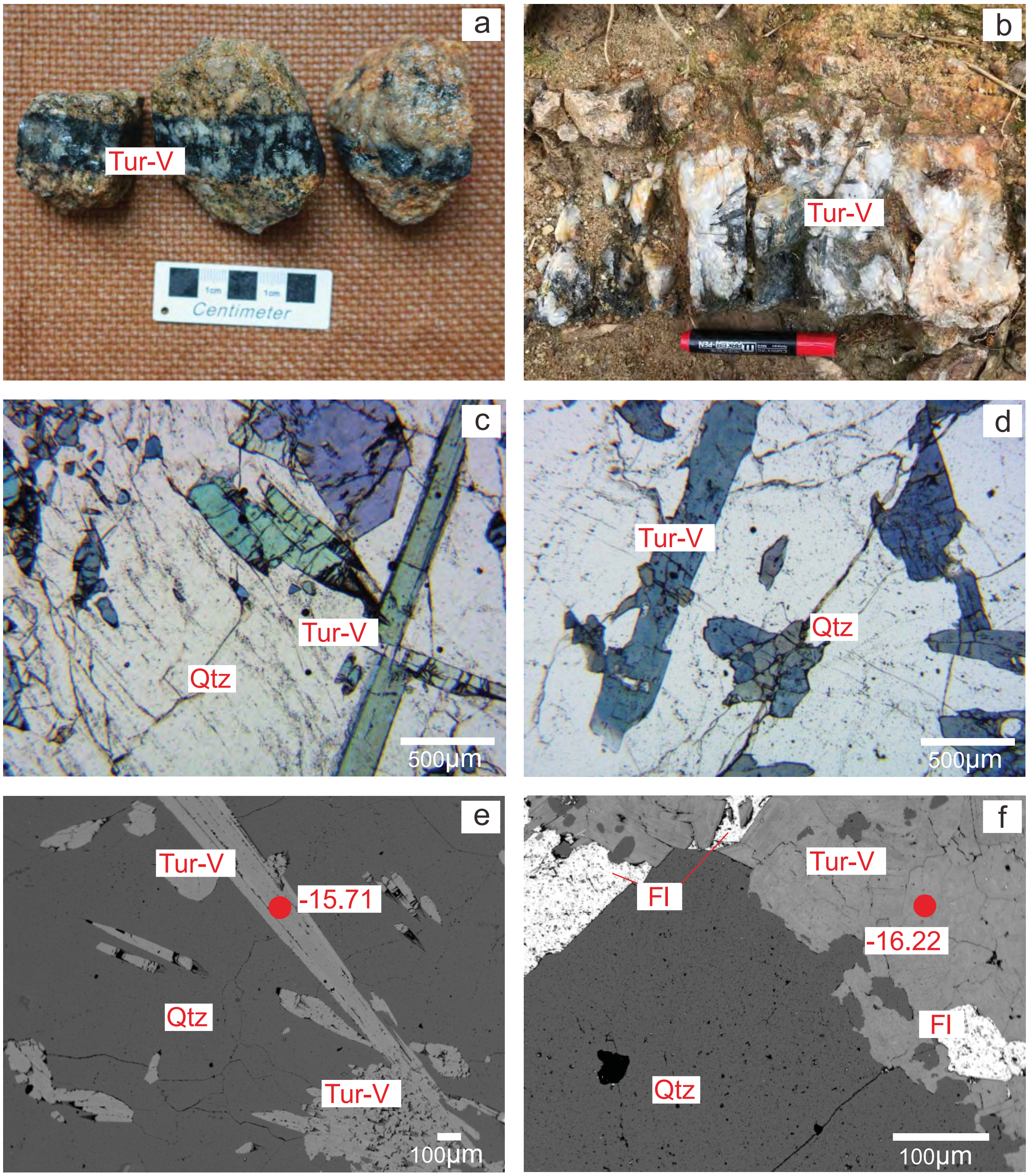

Figure 6

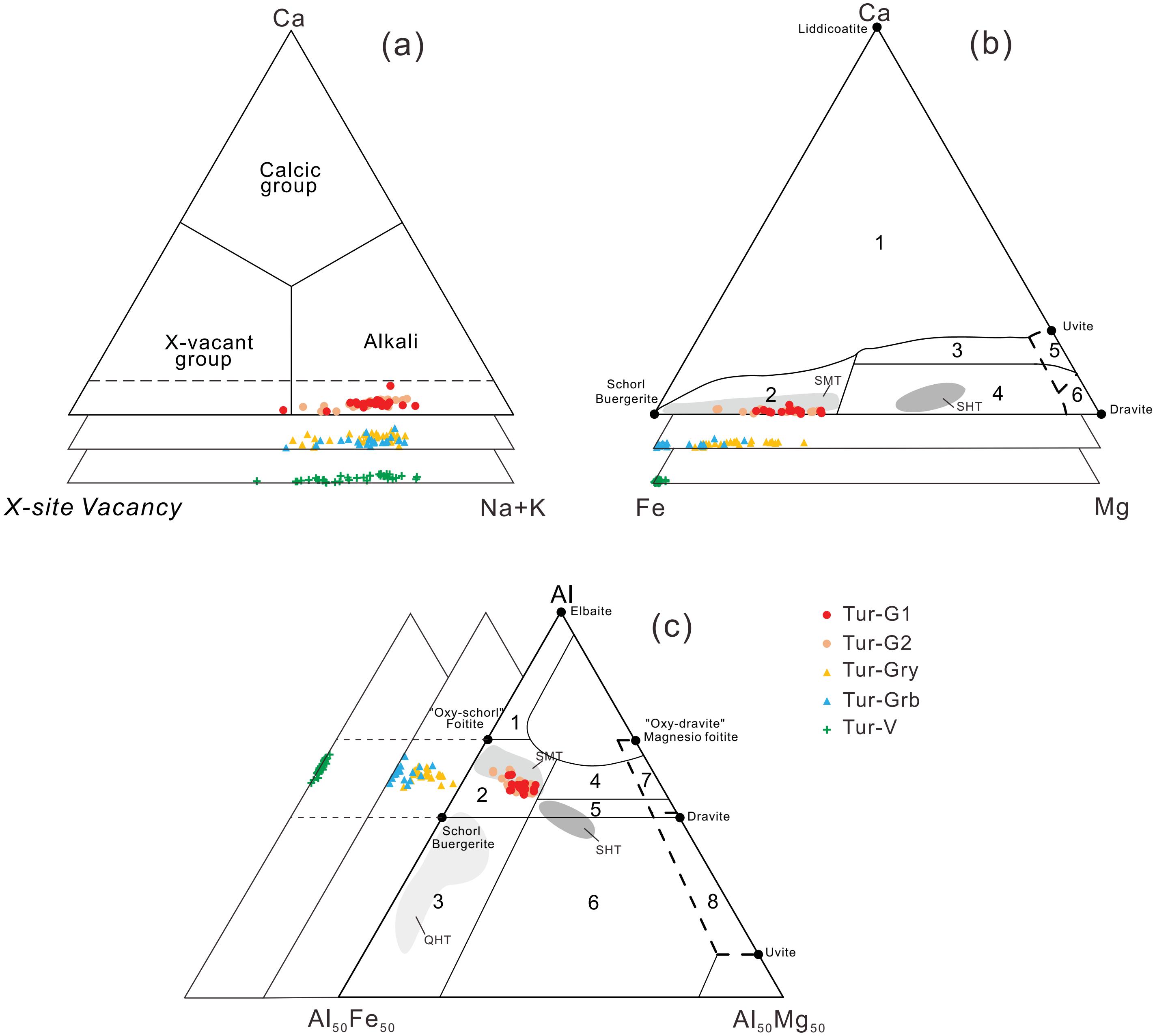
Ca
(a)
Calcic group
X-vacant group
Alkali
X-site Vacancy
Na+K
Ca
Liddicoatite
(b)
1
Uvite
3
5
Schorl
Buergerite
2
SMT
4
6
SHT
Dravite
Fe
Mg
Al
Elbaite
(c)
"Oxy-schorl"
Foitite
1
"Oxy-dravite"
Magnesio foitite
SMT
4
7
2
5
Dravite
Schorl
Buergerite
SHT
3
6
8
QHT
Uvite
Al50Fe50
Al50Mg50
Tur-G1
Tur-G2
Tur-Gry
Tur-Grb
Tur-V

This is the peer-reviewed, final accepted version for American Mineralogist, published by the Mineralogical Society of America.
The published version is subject to change. Cite as Authors (Year) Title. American Mineralogist, in press.
DOI: https://doi.org/10.2138/am-2021-7591. http://www.minsocam.org/

Figure 7

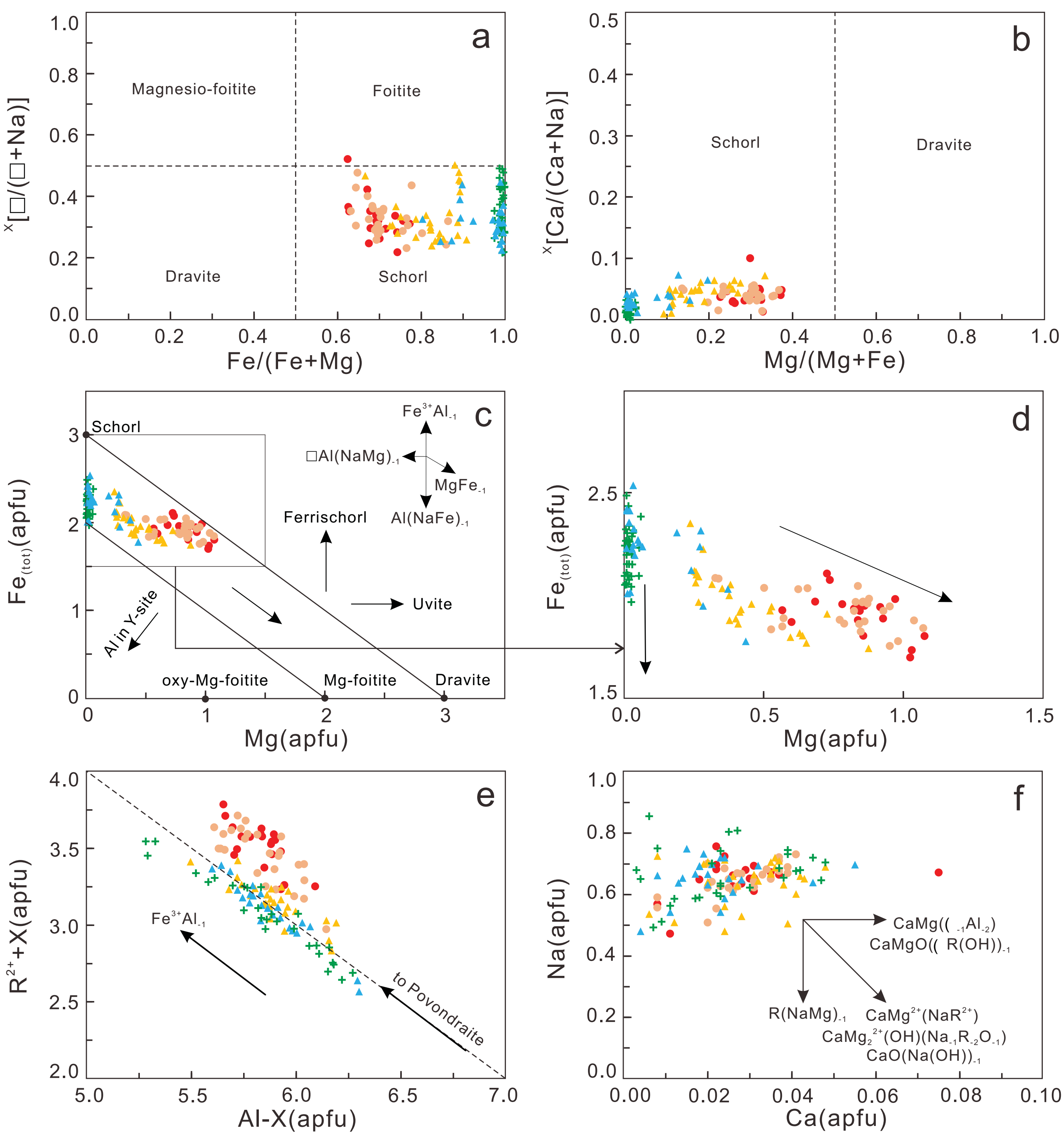

DOI: https://doi.org/10.2138/am-2021-7591. http://www.minsocam.org/

Figure 8

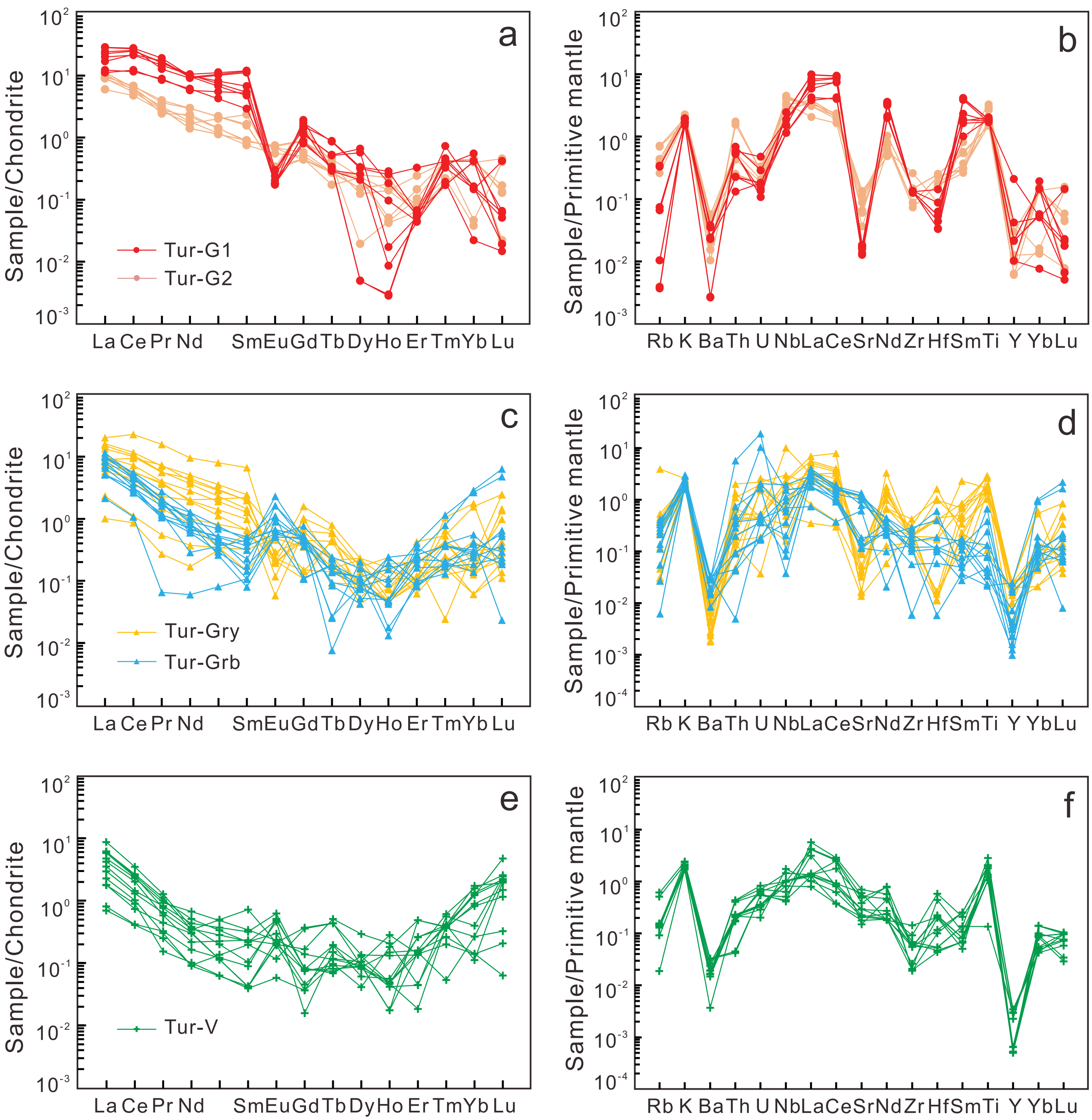

This is the peer-reviewed, final accepted version for American Mineralogist, published by the Mineralogical Society of America.
The published version is subject to change. Cite as Authors (Year) Title. American Mineralogist, in press.
DOI: https://doi.org/10.2138/am-2021-7591. http://www.minsocam.org/

Figure 9

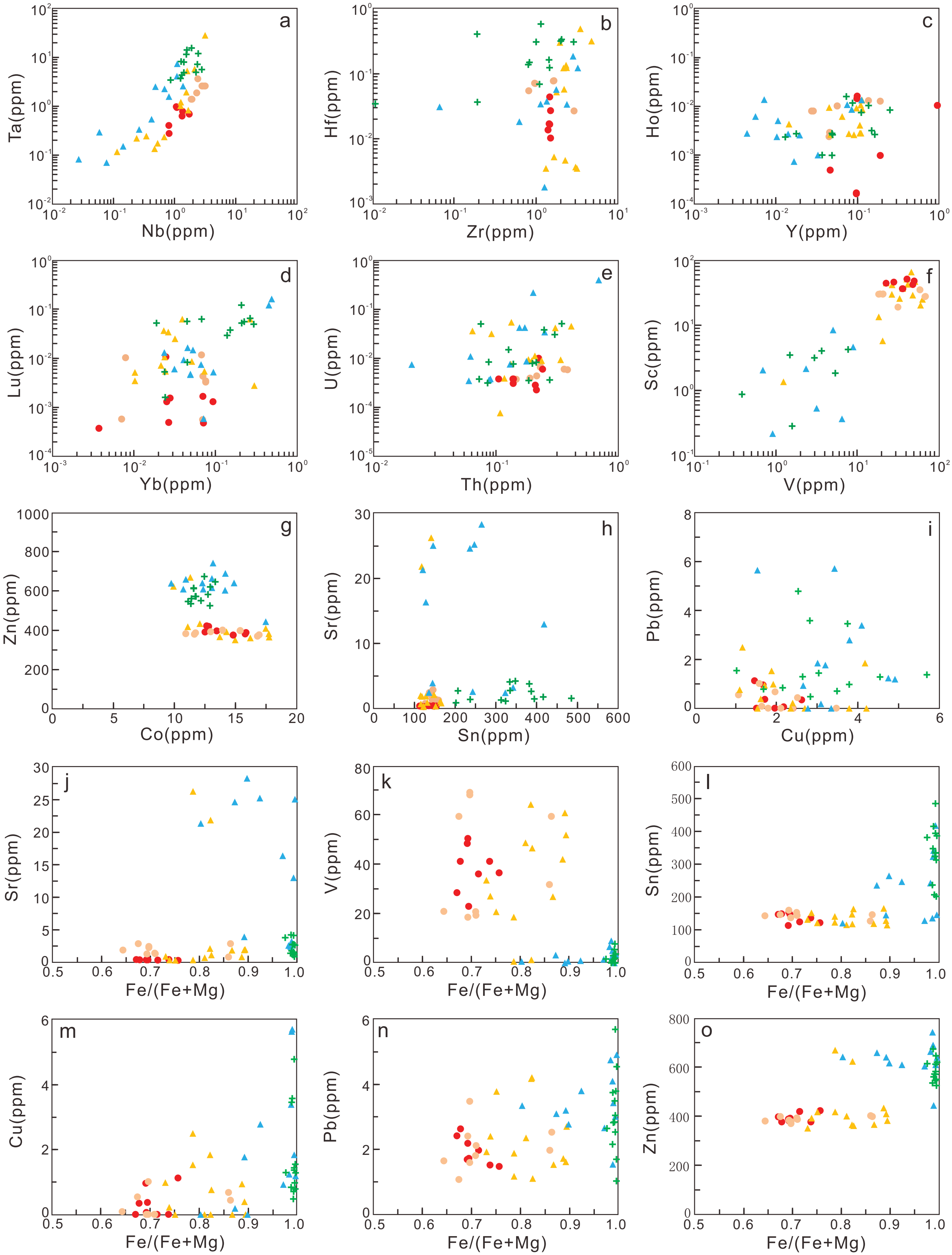

This is the peer-reviewed, final accepted version for American Mineralogist, published by the Mineralogical Society of America.
The published version is subject to change. Cite as Authors (Year) Title. American Mineralogist, in press.
DOI: https://doi.org/10.2138/am-2021-7591. http://www.minsocam.org/

Figure 10

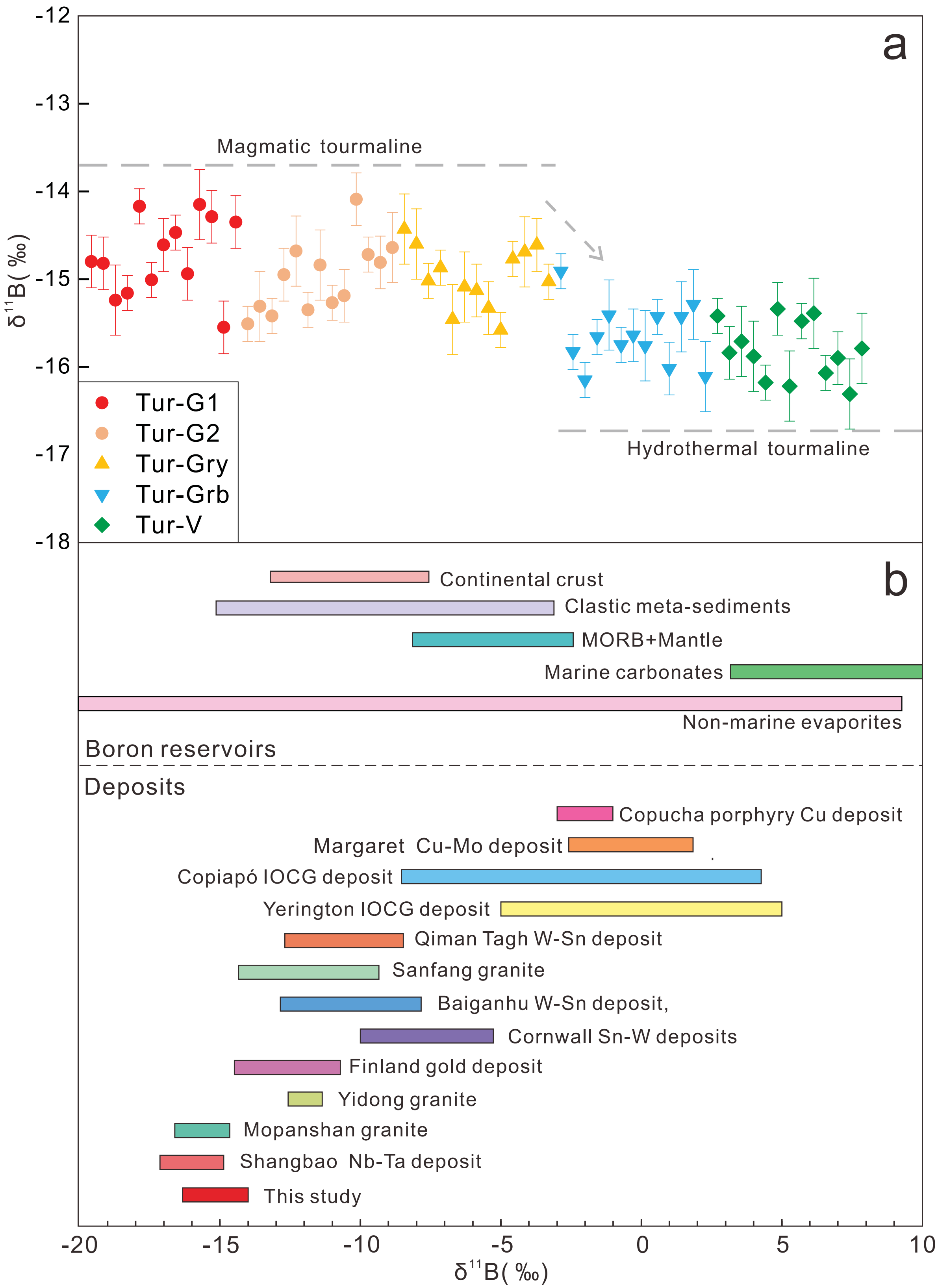

This is the peer-reviewed, final accepted version for American Mineralogist, published by the Mineralogical Society of America.
The published version is subject to change. Cite as Authors (Year) Title. American Mineralogist, in press.
DOI: https://doi.org/10.2138/am-2021-7591. http://www.minsocam.org/

Figure 11